HHS Public Access

Author manuscript

Glia. Author manuscript; available in PMC 2022 April 09.

Published in final edited form as:

Glia. 2022 April ; 70(4): 768–791. doi:10.1002/glia.24138.

Two distinct types of nodes of Ranvier support auditory nerve function in the mouse cochlea

Clarisse H. Panganiban[1,2], **Jeremy L. Barth**[3], **Junying Tan**[1], **Kenyaria V. Noble**[1], **Carolyn M. McClaskey**[4], **Blake A. Howard**[1], **Shabih H. Jafri**[1], **James W. Dias**[4], **Kelly C. Harris**[4], **Hainan Lang**[1]

[1]Department of Pathology and Laboratory Medicine, Medical University of South Carolina, Charleston, South Carolina, USA

[2]Wolfson Centre for Age-Related Diseases, King's College London, London, UK

[3]Department of Regenerative Medicine and Cell Biology, Medical University of South Carolina, Charleston, South Carolina, USA

[4]Department of Otolaryngology & Head and Neck Surgery, Medical University of South Carolina, Charleston, South Carolina, USA

Abstract

The auditory nerve (AN) of the inner ear is the primary conveyor of acoustic information from sensory hair cells to the brainstem. Approximately 95% of peripheral AN fibers are myelinated by glial cells. The integrity of myelin and the glial-associated paranodal structures at the node of Ranvier is critical for normal AN activity and axonal survival and function in the central auditory nervous system. However, little is known about the node of Ranvier's spatiotemporal development in the AN, how the aging process (or injury) affects the activity of myelinating glial cells, and how downstream alterations in myelin and paranodal structure contribute to AN degeneration and sensorineural hearing loss. Here, we characterized two types of Ranvier nodes— the axonal node and the ganglion node—in the mouse peripheral AN, and found that they are distinct in several features of postnatal myelination and age-related degeneration. Cellular, molecular, and structure–function correlations revealed that the two node types are each critical for different aspects of peripheral AN function. Neural processing speed and synchrony is associated with the length of the axonal node, while stimulus level-dependent amplitude growth and action potentials are associated with the ganglion node. Moreover, our data indicate that dysregulation of glial

Correspondence Hainan Lang, Department of Pathology and Laboratory Medicine, Medical University of South Carolina, 165 Ashley Avenue, PO BOX 250908, Charleston, SC 29425, USA. langh@musc.edu.

AUTHOR CONTRIBUTIONS

H.L. and C.H.P. designed the research; C.H.P., J.T., K.V.N., C.M.M., B. A.H., S.H.J., J.L.B., and H.L., performed the research; C.H.P., J.W.D., K. C.H., J.L.B., and H.L. analyzed data; and C.H.P., J.L.B., and H.L. draft the paper.

CONFLICT OF INTEREST

The authors declare no competing financial interests.

DATA AVAILABILITY STATEMENT

The data that supports the findings of this study are available in the supplementary material of this article.

SUPPORTING INFORMATION

Additional supporting information may be found in the online version of the article at the publisher's website.

cells (e.g., satellite cells) and degeneration of the ganglion node structure are an important new mechanism of age-related hearing loss.

Keywords

age-related hearing loss; auditory nerve; glial cells; myelination; nodes of Ranvier; postnatal development; satellite cells

1 | INTRODUCTION

Proper passage of electrical impulses and the regulation of conduction velocity through the peripheral auditory nerve (AN) are crucial for the effective, precise transfer of sound information from the cochlea to the brainstem. Cochlear glial cells enwrap AN fibers and cell bodies with multi-layered myelin sheaths during postnatal development (Romand & Romand, 1990). The formation of myelin sheaths occurs together with the assembly of nodes of Ranvier at the naked gaps between myelin sheaths along axons. There are at least three microdomains in the nodal region: (1) The node, which contains clusters of voltage-gated sodium channels (VGSCs) required for action potential regeneration, (2) the paranode flanks, where the myelin lamellae terminate and provide a physical barrier between ion channels in the node and juxtaparanodes, and (3) the juxtaparanodes, where voltage-gated potassium channels cluster (Arancibia-Cárcamo & Attwell, 2014; Boyle et al., 2001; Eshed et al., 2005; Rasband & Peles, 2016; Susuki et al., 2013). The axo-glial connection is accomplished by cell adhesion molecules such as Cntn1. Together with the myelin sheath, these nodal microdomains are needed for generating and propagating action potentials and maintaining rapid conduction velocity (Boyle et al., 2001; Rasband et al., 1998; Rios et al., 2000). The clustering of VGSCs in the node significantly enhances the efficiency of nerve conduction velocity (Harris & Attwell, 2012). Studies with simulation modeling suggest that node and internode lengths can be fine-tuned to enhance conduction velocity in a rapid, energy-efficient manner (Arancibia-Cárcamo et al., 2014; Ford et al., 2015), although this interesting finding needs to be further validated with experimentally manipulated approaches and in different nervous tissues.

Abnormal development or disruption of the nodal and paranodal microdomains contributes to a wide range of neurological diseases (Susuki, 2013). While there is abundant information about molecular microdomains in the node of Ranvier in other nervous systems (Crawford et al., 2009; Devaux & Scherer, 2005), the study of node microdomains in the peripheral auditory system is very limited. Early electron microscopic studies detected several ultrastructural differences in myelin sheaths around spiral ganglion cell bodies versus those around axons, and detected nodal structure differences on the spiral ganglion neuron (SGN) side compared to the distal side (Rosenbluth, 1962). Later immunostaining assays revealed that the arrangement and maturation of voltage-gated ion channels are important for saltatory conduction in axon initial segments and axonal nodes of the cochlea (Hossain et al., 2005; Kim & Rutherford, 2016). These molecular investigations also reported on the protein expression patterns in the axonal nodes of the AN. However, it remains unclear how the nodes, with their special characteristics, form during development and how they

influence AN function and hearing onset. Here, we characterized these two distinct types of Ranvier nodes— the axonal node and the ganglion node—in the peripheral AN. In this study, the nodes directly flanking either side of the SGN soma in the AN were designated as "ganglion nodes" due to their position. Our data also highlighted the differing myelination characteristics of the two cochlear glia cells—Schwann cells and satellite cells—and their role in axonal (Schwann) and ganglion (satellite) node formation. These data illustrate how these distinct nodes fulfill unique functions in AN function.

Loss or dysfunction of the AN fibers is a key cause of sensorineural hearing loss, the most common type of hearing loss. Extrinsic factors such as exposure to noise and aging can cause degeneration of AN fibers and SGNs (Bao & Ohlemiller, 2010; Liberman, 2017; Liberman & Kujawa, 2017; Spoendlin, 1984). Previous studies showed an initial consequence of noise exposure is a loss of cochlear synapses, which occurs before degeneration of other structural elements in the inner ear (Kujawa & Liberman, 2006; Liberman, 2015; Liberman & Kujawa, 2017; Lin et al., 2011). This finding highlighted the importance of AN degeneration in the etiology of hearing loss. Approximately 90%–95% of AN fibers are myelinated by glial cells. Dysregulation of glial cells in the AN in several pathological conditions is associated with hearing impairment (Akil et al., 2015; El-Badry et al., 2007; Jyothi et al., 2010; Kurioka et al., 2016; Panganiban et al., 2018; Rattay et al., 2013; Tang et al., 2006; Wan & Corfas, 2017). However, the link between the disruption of nodal microdomains and AN functional deficiency in sensorineural hearing loss is largely unknown. Using a mouse model of age-related hearing loss, we found structural abnormalities in the node of Ranvier in ANs of aged mice. Specifically, we discovered changes in the satellite cell-associated ganglion node, implicating glial dysfunction as a mechanism of age-related hearing loss.

2 | MATERIALS AND METHODS

2.1 | Animals

All aspects of animal research were conducted in accordance with the guidelines of the Institutional Animal Care and Use Committee of the Medical University of South Carolina (MUSC). CBA/CaJ mice, originally purchased from the Jackson Laboratory (Bar Harbor, ME), were bred in a low-noise environment at the Animal Research Facility at MUSC. The CBA/CaJ mouse strain is commonly used for normal hearing studies due to their lack of genetic mutations related to hearing and their ability to age without progressive hearing loss (Ohlemiller et al., 2010). Postnatal male and female CBA mice aged postnatal (P) 0, 3, 7, 10, 14, 21, and 1 month (M) were used for the developmental studies. Young adult (1.5–3 months) and aged (2– 2.5 years) CBA/CaJ mice were used in the age-related hearing loss study. Young adult B6.Cg-Gt(ROSA)26Sor$^{tm14(CAG-tdTomato)Hze/J}$ (tdTomato) and B6.Cg-Tg(Plp1-cre/ERT)3Pop/J (Plp/CreER^{T}) mice were bred together and maintained at the Animal Research Facility at MUSC from the breeding strains obtained from the Jackson Laboratory (Bar Harbor, ME). The tdTomato(+/−)/Plp- CreER^{T} (+/−) mice were injected with 1 mg Tamoxifen (Sigma) dissolved in corn oil per 20 mg body weight from P6 to P10 to induce fluorescence in peripheral glial cells. Male and female tdTomato(+/−)/Plp-CreER^{T} (+/−) mice at P13-P14 were used for the isolation of AN glial RNAs. The numbers

of animals per experimental group are reported in the figure legends. All mice received food and water ad libitum and were maintained on a 12-hour light/dark cycle. Mice with signs of external ear canal and middle ear obstruction or infection were excluded.

2.2 | Physiological procedures

For measurements of auditory function, animals were anesthetized via an intraperitoneal injection of a cocktail containing 20 mg/kg xylazine and 100 mg/kg ketamine. Auditory tests were performed in a sound-isolation booth. Equipment for auditory brainstem measurements was professionally calibrated before use with Tucker-Davis Technologies (TDT) RPvdsEx software (TDT, Gainsville, FL) and a model 378C01 ICP microphone system (PCB Piezotronics, Inc; Depew, NY). In a closed-field setup, sound stimuli were delivered into the ear canal via a 3–5-mm diameter tube.

Trial-averaged ABRs were collected using TDT System III and processed with their SigGen software package (Version 4.4.1) as previously described (Panganiban et al., 2018). Stimuli were evoked at pure-tone frequencies of 4, 5.6, 11.3, 16, 22.6, 32, 40, and 45.2 kHz. The stimuli consisted of 1.1-ms tone pips with $\cos^2$ rise-fall times of 0.55 ms and were delivered 31 times/s with a period of 32.26 ms. Responses were collected from 90 to 10 dB SPL sound intensity levels, with each succeeding level reduced in a 5 dB step. The average ABR waveform for each level tested consisted of 256 trials. Results for each mouse were analyzed for wave I response threshold. Thresholds were then averaged at each frequency and the mean ± standard error of the mean was calculated and plotted using Origin 6.0 software (OriginLab Corporation, Northampton, MA).

2.3 | Single-trial recording for ABR metrics analysis

The procedure for continuous single-trial recording was modified from our recent report (McClaskey et al., 2020). For the mice at P14 and P21 used for structure–function correlation analyses, recorded ABRs were elicited only at the 11.3 kHz frequency. Stimuli were 1.1 ms in duration with 0.55-ms $\cos^2$ rise-fall times and were presented at a rate of 21 times/s. Stimuli were presented from 90 to 10 dB SPL in 5 dB SPL decrements. At least 500 tone pips at each sound level were presented. Continuous ABR responses were stored and processed offline in MATLAB (MathWorks, Inc., Natick, MA) using the EEGlab toolbox (Delorme & Makeig, 2004) and the ERPlab extension (Lopez-Calderon & Luck, 2014). Continuous data were bandpass filtered between 100 Hz and 3000 Hz using an 8th order Butterworth filter. Data were then epoched from −3 to +11 ms relative to stimulus onset and baseline corrected using the baseline subtraction method with a pre-stimulus window of −3 to −1 ms. Epochs with voltages exceeding +/− 5 μV were rejected and the remaining epochs were visually inspected for excessive movement or other artifacts. Artifact-free trials were saved in the single-trial form in EEGlab and as a trial-averaged ABR waveform in ERPlab. Wave I was visually identified as the first major positive inflection following stimulus onset. Peak amplitude and peak latency were calculated from the trial-averaged ABR waveform and phase-locking value (PLV) was calculated from the single-trial-level data. All measurements were made offline in MATLAB using custom EEGlab and ERPlab functions. Suprathreshold metrics were quantified from responses at 65 dB SPL and above.

Wave I peak amplitude was calculated as the absolute voltage of the wave I peak in microvolts and peak latency was calculated as the latency in ms of the wave I peak. Fractional peak latency (Luck, 2014) is the latency of the point where waveform amplitude has reached 10% of the distance between the wave I start (defined as the local minimum preceding wave I) and wave I peak. The 10% point was used to eliminate the influence of random fluctuations at the start of the waveform (Harris et al., 2018). PLV, also known as inter-trial coherence (ITC), is the length of the vector that is formed by averaging the complex phase angles of each trial at each frequency and was obtained via time-frequency decomposition of the single-trial-level data. Time-frequency decomposition was performed with Hanning FFT tapers via EEGlab's newtimef() function, using 16 linearly spaced frequencies from 190 to 3150 Hz. The PLV at each timepoint and each frequency was then calculated by taking the absolute value of the complex ITC output of the newtimef() function. Mean PLV between 500 and 2500 Hz in the 2-ms window surrounding the wave I peak was then taken as the metric of PLV. A sample PLV time-frequency decomposition is shown in Figure 7a.

2.4 | Collection of cochlear nerve and glial cell enriched tissue and total RNA isolation

Cochleae were collected from mice at their designated end-points. Micro-dissections were performed to isolate the AN from the rest of the cochlear structures, taking care to preserve peripheral fibers. Two cochleae from each mouse were pooled for individual samples. Total RNA was purified from each sample using the miRNeasy Mini Kit (Qiagen Inc, Germantown, MD) per the manufacturer's instructions. The quality of each total RNA isolation was assessed using the Agilent 2100 Bioanalyzer (Agilent Technologies, Santa Clara, CA). Low-quality samples showing degradation or contamination were excluded.

For the preparation of the fluorescent activated cell sorting (FACS) of mouse AN glial cells, the cochleas of tdTomato(+/−)/Plp1-CreER^{T} (+/−) mice at P13-P14 were subjected to micro-dissection in cold HBSS solution for the isolation of the AN and cochlear lateral wall tissues. Two samples were created by pooling the cochleas from three mice (two females and one male) per sample. Samples were then transferred into 4-well plates containing a pre-warmed (≤5 min at 37°C, 5% CO_2) enzymatic digestion solution consisting of 0.5 mg/ml collagenase (Sigma, Cat No. C-1764) and 0.2% trypsin incubated at 37°C for 7 min. Following this, DNase I (1 mg/ml) was added, the mixture triturated three times, and returned to the incubator for another 7 min. After incubation, 10% fetal bovine serum (FBS) in Dulbecco's Modified Eagle's Medium (DMEM) was added to each well to quench the enzymatic digestion. The cells were triturated 40–50 times using a 200 μL pipette to break up clumps and aid tissue dissociation. The mixture was then collected in a 15 ml conical tube (600 μL of combined digestion solution, DNase I, and 10% FBS in DMEM). An additional 10% FBS in DMEM was used to wash the well and collect any remaining cells to the 15 ml tube. Samples were centrifuged at 1.8 rpm for 5 min at room temperature. The cell pellet in each 15 ml tube was resuspended with FACS buffer. Samples were centrifuged for a second time at 1.8 rpm for 5 min at room temperature. The supernatant in each sample was removed and the cell pellet was resuspended in FACS buffer. The cell suspension was passed through a 0.2 μm filter top polystyrene tube for each sample. The 15 ml conical vial was rinsed with an additional 200 μL of FACS buffer and any residual cells were

transferred to the filter tube. All samples and FACS buffer were held on ice until sorting was performed using the FACSAria Ilu cell sorter for enrichment of Plp1 positive glial cells. The FACSAria Ilu cell sorter was controlled by a HP xw4600 workstation running FACSDiva version 6.1.3. Total RNA was purified from each Plp1+ glial samples using the miRNeasy Mini Kit (Qiagen Inc, Germantown, MD) as described above.

2.5 | RNA sequencing

Two RNA sequencing (RNA-seq) studies were performed on AN, one profiling changes associated development and the other profiling changes associated with aging. For the developmental study, P3, 7, 14, 21 and young adult (2 month) CBA/CaJ samples were analyzed. For the aging study, young adult (2 month) and aged adult (2.5 year) CBA/CaJ samples were analyzed. Both studies used total RNA (50 ng) with RNA integrity numbers of >8 and three biological replicates ($n = 3$) per sample type. Library preparation and paired-end next-generation sequencing using the Illumina HiSeq2500 (Illumina, San Diego, CA) was performed by the MUSC Genomics Shared Resource. The resulting FASTq data was processed with Partek Flow™ software. This included alignment with TopHat2, quantification to annotation model (Partek E/M), and normalization and comparison by DeSeq2 (Love et al., 2014), which calculates an adjusted p-value (FDR step up). RNA-seq datasets were deposited in the NCBI Gene Expression Omnibus (development study, GSE133823; aging study, GSE141865). This study used a list of myelin-related genes established and published in our previous study (Panganiban et al., 2018). The gene list that was queried had 1895 unique genes and was compiled from several resources: (1) mRNAs enriched in myelinating oligodendrocytes compared with other cell types including astrocytes, neurons, oligodendrocyte progenitor cells, newly formed oligodendrocytes, microglia, and endothelia in mouse cerebral cortex at FPKM (fragments per kilobase of transcript per million mapped reads) thresholds of 0.1, 1, 10, and 20 (Zhang et al., 2014); (2) mRNAs with normalized read counts of >100 and more than twofold increase in male mouse brain myelin (Thakurela et al., 2016); (3) genes on the mouse 430 2.0 GeneChip (Affymetrix) identified by query for the term “myelin”; and (4) a curated set of genes related to the node of Ranvier. Of the 1895 genes in the myelin-related gene list, 1727 were present in our development data set (Table S3). The list of node-related genes was compiled from a manual literature search (Boyle et al., 2001; Custer et al., 2003) and query of amiGO (Carbon et al., 2009) using the terms “node of Ranvier,” “paranode region of the axon,” “paranodal junction assembly,” “juxtaparanode,” and “internode.” (Table S4).

2.6 | Quantitative PCR

Two-step reverse transcription quantitative polymerase chain reaction (RT-qPCR) was performed by first converting total RNA into cDNA via QuantiTect Reverse Transcription Kit (Qiagen, Germantown, MD). The resulting cDNA was queried for expression of genes of interest and the 18S reference gene via qPCR using TaqMan probes (Applied Biosystems, Waltham, MA) and a Lightcycler 480 (Roche Diagnostics, Indianapolis, IN). Each experiment included a “no reverse transcription” control; reactions were performed in technical triplicate with 40 cycles of 2-step cycling. Amplification efficiency was calculated by standard curve method using 10-fold serial dilutions of cDNA for each target gene; Efficiency was determined by the Equation $E = 10 (-1/S)$, with S as the slope. Relative

expression was calculated using the ΔΔCT method adjusted for calculated efficiencies; measures were normalized based on the 18S amount (Livak & Schmittgen, 2001).

2.7 | Immunohistochemistry

Immunohistochemical procedures were modified from previous studies (Panganiban et al., 2018). After end point physiological recordings, mouse cochleae were collected and immediately fixed with 4% paraformaldehyde solution in 1× phosphate-buffered saline for 2 h at room temperature and decalcified with 0.12 M ethylenediamine tetra-acetic acid (EDTA) at room temperature for 1–2 days. To prepare for cochlear frozen sections, cochleae were embedded in the Tissue-Tek OCT compound and sectioned at a thickness of approximately 10 μm. For whole-mount preparations of mouse cochlear tissues, the ANs and organs of Corti were isolated from the rest of the cochlear structures. Frozen sections of human temporal bones were obtained from sets we collected in previous studies (Hao et al., 2014). Procedures for human cochlear tissue were reported in detail previously (Hao et al., 2014).

The primary and secondary antibodies used for immunohistochemistry are listed in Table S1. Staining was performed by either indirect method using biotinylated secondaries conjugated with fluorescent avidin (Vector Labs, Burlingame, CA) or direct method using Alexa Fluor Dyes (ThermoFisher Scientific, Waltham, MA). Nuclei were counterstained using 4′,6-diamidino-2-phenylindole (DAPI). Slice and confocal image stacks were collected using a Zeiss LSM 880 NLO with ZEN acquisition software (Zeiss United States, Thornwood, NY). Image stacks were taken at 0.75 μm intervals with image sizes of 134.95 μm (x)× 134.95 μm (y). Images were processed using ZEN 2012 Blue Edition (Carl Zeiss Microscopy GmbH) and Adobe Photoshop CC (Adobe Systems Incorporated, San Jose, CA).

2.8 | Identification of nodal structures and measurement of node lengths

Nodal microdomains were marked via immunostaining of either NrCAM or $Na_v1.6$. Paranodal microdomains were marked via immunostaining of Cntn1. Node measurements were acquired using the measurement tool in ZEN. Confocal image stacks were taken at 0.75 μm intervals from 10 μm cochlear frozen sections that were processed into a single-layer maximum intensity projection. Node length was taken as the end to end of NrCAM-marked node (see Figure S5). Fully intact nodes in the parallel plane were measured to limit possible inaccuracies. Straightness and wholeness of the nodal structures were checked using (1) the presence of flanking paranodes, (2) 3D visualization of the tissue section using ZEN, and (3) the range-indicator tool on ZEN.

2.9 | Transmission electron microscopy

Samples were prepared for transmission electron microscopy using procedures modified from previous publication (Lang et al., 2015). Briefly, deeply anesthetized mice were cardiac perfused with a mixture of 10 ml saline and 0.1% sodium nitrite solution, followed by 15 ml of a fixative solution containing 4% paraformaldehyde and 2% glutaraldehyde in 0.1 M phosphate buffer, pH 7.4). The same fixative solution was used to perfuse the excised cochleae through the round window and for further immersion overnight at 4°C.

Cochleae were then decalcified using 0.12 M EDTA solution at room temperature for 2–3 days with a magnetic stirrer. Then, cochleae were fixed using a solution containing 1% osmium tetroxide and 1.5% ferrocyanide for 2 h in the dark. They were then dehydrated and embedded in Epon LX 112 resin. Semi-thin sections for pre-TEM observation of AN orientation were cut at 1-μm thickness and stained with toluidine blue. Once a cochlear middle or basal portion plane was identified, ultra-thin sections at 70-nm thickness were cut and stained with uranyl acetate and lead citrate. These ultra-thin sections were examined using a JEOL JEM-1010 transmission electron microscope (JEOL USA, Inc., Peabody, MA). Myelin thickness, axonal diameter and G ratio were measured using the open-source imaging software, Fiji (RRID:SCR_002285; Paus and Toro, [2009]). These measurements were collected for the axons in the middle- and high-frequency areas of cochleas at P7 and P14. These measurements included 204 axons of the middle cochlear portions from three mice and 144 axons of basal portions from four mice at P7, and 37 axons of the middle portion from 1 mouse at P14.

2.10 | Experimental design and statistical analyses

Sample numbers (n) are indicated in each figure legend. The *n* for physiological measurements (e.g., amplitude and latency) and RT-qPCR studies were based on prior studies (Lang et al., 2015; Xing et al., 2012). For RNA-seq, prior analyses of mouse AN demonstrated that a sample size of $n = 3$ was sufficient for robust detection of differentially expressed genes (Lang et al., 2015). Data distribution was tested using either Shapiro–Wilk or Kolmogorov–Smirnov tests for normality. The appropriate parametric or nonparametric tests were then used. Statistical software and packages used in this project include DeSeq2 (Love et al., 2014), Microsoft Excel, R version 3.5.2 (R Foundation for Statistical Computing, 2019), and/or GraphPad Prism 8 (GraphPad Software, Inc., La Jolla, CA). Statistical relationships were tested for significance at alpha = 0.05 following correction for inflated familywise error. The detailed information of statistical analyses is included in Tables 1–3 and Tables S2, S3, S4, S5, S6, S7 and S8.

3 | RESULTS

3.1 | Myelination of the neuron soma is preceded by axonal myelination during postnatal AN development and hearing onset

The reported onset of hearing (which is defined here as the earliest age hearing threshold is present at the given maximum stimulus level of 90 dB SPL) varies in mouse strains but generally occurs between P9 and P14 (Alford & Ruben, 1963; Ehret, 1976; Song et al., 2006; Sonntag et al., 2009). In the CBA/CaJ mice used in this study, the external auditory meatus often opened at P11. Maturation of suprathreshold hearing function continues following the onset of hearing. To confirm the critical time points of postnatal development of AN and hearing onset in these mice, an auditory brainstem response (ABR) was measured at P12, P14, P21, and 1 M (Figure 1u, Table S2). Reliable ABRs with a clear wave I peak were recorded starting at P12. By P14, the ABR wave I thresholds improved approximately 25 to 30 dB across the frequencies tested. Threshold responses were significantly improved between each successive age group, except for P21 versus 1 M for most frequencies tested, suggesting that hearing sensitivity reached maturity by P21. At P21 and 1 M, ABR

thresholds approximated those observed in young adult CBA/CaJ mice (Liu et al., 2019; Xing et al., 2012). These ABR data confirmed that the time points of P14, P21, and 1 M constituted an appropriate developmental continuum to evaluate AN structure and its relationship to hearing onset.

To better understand how nodal structures form in the AN, we examined ultrastructural features of myelination in the cochleas of CBA/CaJ mice at stages before hearing onset (P0, P3, P7, and P10) and after hearing onset (P14, P21, and 1 M; Figure 1u) using TEM (Figure 1). Myelin sheaths formed around the AN axons at P7 and older stages (Figure 1c-g,I,j,i-m), but not at P0 (Figure 1a) or P3 (Figure 1b). By P7, the thickness of the Schwann-cell processes surrounding the axons varied in both the middle- (Figure 1e,f) and high-frequency (Figure 1d) areas of the cochleas. The myelin thicknesses, axonal diameters, and G ratios in the middle portions of the cochleas at P7 ranged from 0.12 to 0.28 μm (mean = 0.20 μm), from 0.97 to 1.59 μm (mean = 1.28 μm) and from 0.69 to 0.83 (mean = 0.69), respectively. Similarly, the myelin thicknesses, axonal diameters, and G ratios in the basal portions of the cochleas at P7 ranged from 0.12 to 0.32 μm (mean = 0.22 μm), from 0.97 to 1.59 μm (mean = 1.28 μm) and from 0.64 to 0.82 (mean = 0.73), respectively. In agreement with our previous observations (Brown et al., 2017), the AN refinement was evident at P7 by the macrophage activation (a black arrow in Figure 1e) and glial-like cell proliferation (a black arrowhead in Figure 1f). Variation in myelin thickness and their axon diameter diminished with an increased myelin thickness after P10. For example, the myelin thicknesses, axonal diameters, and G ratios in the middle portions of the cochleas at P14 ranged from 0.25 to 0.45 μm (mean = 0.35 μm), from 0.73 to 1.27 μm (mean = 1.00 μm) and from 0.51 to 0.75 (mean = 0.63), respectively (Figure 1j). By P21 (Figure 1m, the boxed area in Figure 1o), myelination was mostly complete, with myelin sheath thickness similar to that observed in 1M old mice (Figure 1r) and young adult mice reported previously (Lang et al., 2011; Xing et al., 2012). The myelin features of the SGN somata are clearly different compared to those of the axons in both thickness of myelin sheaths and timing of myelination. Myelination of SGN somata began at P10, about 3–5 days later than myelination of the axons, with only 2 to three layers of thick, cytoplasm-filled satellite-cell processes seen around the neuron cell bodies (Figure 1h,i). Although the glial cells that myelinate SGNs could actually be Schwann cells that respond differently to distinct molecular signals from the soma compared to those on the axon, we designated these glial cells as satellite cells because the similar cell type that ensheathes sensory neuron somata are commonly termed “satellite cells” (Hanani, 2005). By P14, the layers of satellite cell processes increased but no compact myelin sheaths were formed (Figure 1k). The compact myelin sheath is composed of multiple dense membranes of myelin lamellae with very little cytoplasm and can be clearly identified in the EM graphs by their fine structure (between the white arrows in the inner box in Figure 1t; seen with higher magnification). With a lower magnification EM image, each lamellae in the compact sheath appears as thin, dark lines (between the white arrows in Figure 1t). Compact myelin sheaths were detected around neurons at P21 and 1 M (Figure 1j-m,o,p).

Together, our EM observations suggest that (1) myelination of AN axons by Schwann cells begins around P7 and is completed around P14; (2) myelination of SGN soma by satellite cells, another type of glial cell in the cochlea, starts shortly before hearing onset at P10, and is completed by P21; (3) an approximately 7-day delay occurs between the formation

of the compact myelin sheath around axons (by Schwann cells) and around the somata (by satellite cells), and (4) the glial cells of the AN show distinct function in their roles in AN myelination in SGNs (the satellite cells) and axons (the Schwann cells), respectively.

3.2 | Expression profiles of genes composing nodal structural microdomains exhibit special temporal patterns in the developing AN

To characterize nodal assembly processes during postnatal AN development and hearing onset, we examined the expression profiles of myelin- and node-related genes at several critical developmental time points of myelination, including P7, P14, and P21. These timepoints were identified in our TEM studies (Figure 1). P3 was also selected as a control for the pre-myelinated AN. Analyses of AN RNA-seq data from these critical time points showed that 1502 of 1727 myelin-related genes were significantly regulated (p adjusted <.05 for at least one pairwise comparison) (Figure 2a; Table S3). The list of 1727 myelin-related genes used for this analysis was described in our previous study (Panganiban et al., 2018). Three key myelin related molecules among the 1502 identified myelin-related genes, *Plp1*, *Sox10*, and *Qk*, have been well-studied in the mouse AN (Lang et al., 2011, 2015; Panganiban et al., 2018; Wan & Corfas, 2017). As shown in Figure 2b, validation of the expression of *Plp1*, *Sox10* and *Qk* was performed with RNA samples obtained from glial cells and nonglial cells of mouse AN via RT-qPCR. The localization of QK protein was also revealed in glial cells of the AN via immunostaining assay (Figure 2c). Additionally, 38 of the 42 genes identified as node-related were differentially expressed during this developmental period (Figures 2–3). Hierarchical clustering of expression data for the node-related genes revealed that the genes were separable into three different clusters of temporal expression profiles (Figure 2d). Cluster 1 (peak expression P3-P7) contained genes important for the onset of nodal microdomain formation, including those affecting cell–cell interaction, scaffolding, cell adhesion, and extracellular matrix (Custer et al., 2003; Ervasti & Campbell, 1993; Woods et al., 1996). Cluster 1 also contained Scn2a, which encodes the VGSC $Na_v1.2$. This channel protein is a marker of immature nodes and is later replaced by robust expression of $Na_v1.6$ (encoded by *Scn8a*). $Na_v1.6$ is one of the VGSCs identified in nodes of the peripheral nervous system after the onset of myelination (Kaplan et al., 2001; Schafer et al., 2006; Luo et al., 2014). Cluster 2 (peak expression at P7-P21) contains genes involved in the onset of paranodal junction assembly (Eylar et al., 1971; Ishibashi et al., 2004; Kwon et al., 2013; Li et al., 1994; Orthmann-Murphy et al., 2009; Quarles et al., 1973; Snipes et al., 1992; Zonta et al., 2008). This cluster includes *Cntn1*, which encodes the *Cntn1* axo-glial connector protein that attaches axolemma and myelin lamellae at the paranode (Boyle et al., 2001). Cluster 3 (peak expression at P14–21) is comprised of genes encoding structural proteins of the electrically excitable nodal microdomain (Huang et al., 2017; Lacas-Gervais et al., 2004), and axo-glial connector proteins at the paranode (Rios et al., 2003) and juxtaparanode (Poliak et al., 1999; Poliak & Peles, 2003). Cluster 3 also included genes encoding voltage-gated potassium channels of the juxtaparanode (Rasband et al., 1998; Rasband & Trimmer, 2001) and the mature nodal $Na_v1.6$. These gene expression patterns support the scheme that node formation begins around P3, paranodal microdomain formation and myelination begin around P7, and juxtaparanode assembly begins around P14. This time-dependent up-regulation of genes encoding nodal structural proteins and

voltage-gated ion channels suggests that the nodes of Ranvier develop before hearing onset and have fully formed microdomains by the time of hearing onset.

As shown in Figure 2d–h, our RNA-seq findings were validated by immunostaining and RT-qPCR. NrCAM node protein, which is encoded by *Nrcam* and needed for node assembly (Custer et al., 2003; Feinberg et al., 2010), was detected in ANs at P3 and P10 (Figure 1d). Dual-immunostaining analysis with NrCAM and neuronal marker NF200 showed that NrCAM is present very early in nodes of the mouse AN (Top panels of Figure d). At P3, NrCAM was present only in the hook area of the AN, which is the basal-most point of the cochlea. This may indicate that nodal assembly occurs in a basal to apical gradient, which would be consistent with the basal to apical development pattern of other cochlear structures. Dual-immunostaining analysis with NrCAM and the paranodal protein Cntn1 revealed that distinct nodal ($NrCAM^+$) and paranodal ($Cntn1^+$) microdomains were present at P10 (Bottom panels of Figure 1d). With RT-qPCR analysis, we assessed the temporal expression pattern of node-related genes in Cluster 2 (*Cntn1*; Figure 2e) and Cluster 3 (*Cntnap1*, *Kcna2*, and *Scn8a*; Figure 2f–h). Our statistical analysis confirmed that all genes were significantly upregulated between P3 and P14 (one-way ANOVA with Bonferroni post hoc adjustment; Table 1).

Heminodal clustering in the postnatal AN occurs in a spatially and temporally dependent manner. In the central nervous system, action potentials are generated at the axon initial segment, a site located between the neuron cell body and the axon process (Palay et al., 1968). However, the generation of action potentials in the peripheral AN has not been fully understood. The inner hair cells (IHCs) are innervated by the peripheral processes of SGNs, whose bipolar cell bodies are located within Rosenthal's canal (Figure 1r; Left panel of Figure 4). Several spike-generating Na_V and K_V channel proteins have been identified at multiple sites along the peripheral AN (Hossain et al., 2005; Kim & Rutherford, 2016). These sites include nodal microdomains in the peripheral axons and the heminodes.

Heminodes at the habenula under the IHCs of the adult mouse form in part the cochlear axon initial segment and are located on the distal end of type I SGNs. These nodal structures are 20–40 μm from the presynaptic ribbon-type active zone on an IHC (Hossain et al., 2005; Liberman, 1980). A previous study using computational modeling of patch-clamp recording from rodent ANs revealed that action potentials of the AN begin in these heminodes (Rutherford et al., 2012). To study heminodes formation in postnatal cochleas, immunostaining was conducted on whole-mount AN tissue preparation from mice at ages P7, P10, P14, and 1 M ($n = 3$ mice per age group) for the nodal markers NrCAM or Nav1.6, together with the paranodal marker Cntn1 (Figure 3). Our data showed that before P14, the molecular components of the heminodes (as marked by NrCAM or Nav1.6) are still positioned towards the habenula (Figure 3a-a",b-b",e,f). This is less apparent in the basal turn at P7 (Figure 3a"), as more $NrCAM^+$ heminodes are finally clustered underneath the IHCs. Clustering of the heminodes, and the movement of the heminodal components towards the habenula is driven by axonal myelination. While several heminodes visibly approach from the osseous spiral lamina (OSL) region in the basal turn at P7, heminodes are almost completely clustered under IHCs in the basal turn at P10 (Figure 3b"). The number of unclustered heminodes approaching the habenula from the OSL is even more apparent

in the middle turn at P7 to P10 (Figure 3a',b') and in the apical turn at P7 to P14 (Figure 3a–c). By P14, the close clustering of heminodes underneath IHCs is mostly complete in the basal and middle turns. In ANs of 1 M young-adult mice, heminodal clustering is complete in all three turns (Figure 3d,d',d"). These observations support the conclusion that heminode migration and clustering underneath the IHCs progresses along the cochlear turns in a basal to apical direction. The flanking Cntn1^{+} paranode also shows the position of the heminodal component towards the habenula during P7 to P14 and highlights the distance between the heminode clusters and the first axonal node. As shown in Figure 3e-h, the heminode clustering completes in the middle turn by P14 as the clusters are directly under the IHCs. In agreement with the previous observation, we also showed expression of NrCAM protein in sensory hair cells at P7 and P14 (Figure 3 a, a', a",b,b',b"; Harley et al., 2018).

3.3 | Assembly patterns of nodal and paranodal proteins reveal the formation of two distinct types of nodal microdomains in the AN

To study nodal structure formation in postnatal AN, we performed dual-immunostaining for nodal NrCAM and the paranodal Cntn1 on frozen sections prepared from cochleas at P7, P10, and P14 (Figure 4). Frozen section imaging corroborated our finding from whole-mount preparations regarding the heminode clustering region in Figure 3. Along AN passing through the OSL, Rosenthal's canal, and central modiolus region (Mod), two types of nodes of Ranvier were seen: (1) axonal nodes positioned along the peripheral AN processes at the AN within the OSL and the central process at the Mod (Figure 4a,e,I,b,f,j,c,g,k); and (2) ganglion nodes, found flanking type I SGN somata in Rosenthal's canal (Figure b,f,j,d,h,l). At P7, axonal nodes (NrCAM^{+}), are present and appear to be flanked by two partially formed paranodes (Cntn1^{+}) (Figure 4c). In contrast, most ganglion node paranode flanks on the side of the somata have little to no Cntn1 immunoreactivity (Figure 4d). By P10, axonal nodes express Cntn1 on both paranodal domain positions (Figure 4g). Cntn1 activity was also seen in the axonal paranode flank but not in the ganglion paranode flank on the soma side of the ganglion nodes (Figure 4h). Other ganglion nodes at P14 show little presence of Cntn1 in the ganglion paranode flank compared to the robust presence of Cntn1 in the axonal paranode flank (Figure S5b). Differential expression pattern of Cntn1 in ganglion nodes and axonal nodes may be associated with the difference in myelination in neuronal cell bodies and axons. Depletion of paranodal adhesion molecules (such as Cntn1 or Neurofascin) results in mistargeting of myelin to cell bodies (Djannatian et al., 2019; Klingseisen et al., 2019). It is possible that a lack or decreased presence of Cntn1 in the ganglion paranode flank compared to the axonal paranode flank contributes to the smaller number of myelin lamellae ensheathing the somata. By P14, we saw distinct immunostaining patterns of nodal (Cntn 1^{+}) and paranodal (NrCAM^{+}) elements in the axonal node and ganglion node (Figure 4k,l). This staining pattern was maintained in cochleas of P21 (Figure 4m,n), young-adult (Figure 5m,n) and aged mice (Figure 8a), and was also seen in the aged human temporal bone (Figure 8c). We also observed a similar staining pattern with nodal (Cntn 1^{+}) and paranodal (Nav1.6^{+}) (Figure 4q,s; Figure S2). In addition, our immunostaining with Caspr antibody revealed Caspr^{+} paranodes of the AN axons at P21 mice, however, the axonal Caspr immunostaining is much weaker than that of the Cntn1 immunostaining in the same region (Figure 4m-p).

Taken together, these data demonstrated distinct features of two types of nodal structures with unique features in the AN: (1) there are two robustly Cntn1$^+$ paranodal elements in the axonal node, whereas the ganglion node contains one robust Cntn1$^+$ paranodal element, with the paranode flank on the soma side containing little to no Cntn1; and (2) the NrCAM$^+$ nodes are significantly shorter in axonal nodes than ganglion nodes (unpaired *t* tests, $p < .0001$) (Figure 6 and Table 2). The difference in nodal structure also occurred in all reported axonal node lengths when compared to corresponding ganglion node lengths from the same age group and cochlear turn (e.g., P7 apical axonal node vs P7 apical ganglion node). In addition, the delay in ganglion node development compared to the axonal node corresponds with a similar delay in myelination of soma, in contrast to peripheral axons (Figure 1).

3.4 | Axonal and ganglion paranodes in the postnatal AN have different axo-glial connection patterns dependent on the type of myelinating glia

Axonal paranodes are generated by the terminus of the myelin lamellae from myelinating Schwann cells at the paranodal axolemma. Unlike the thin, nearly cytoplasm-free myelin lamellae ensheathing the internodes, the terminating lamellar loops at the paranode are filled with cytoplasm. These loops provide a larger surface area for axo-glial connections and glial-glial connections between the adjoining lamellae and terminal loops (see reviews by Poliak & Peles, 2003; Sherman & Brophy, 2005; Figure 5f, l, o, p). The terminal myelin loops and their axo-glial connections serve as physical barriers that separate the VGSCs in the node from the voltage-gated potassium channels in the juxtaparanode. To better understand the differences in (1) the structure of the two nodal types and (2) the axo-glial interactions in the axonal paranodes (formed by Schwann cells) and ganglion paranodes (formed in part by satellite cells), we analyzed the ultrastructural features of peripheral ANs in postnatal mice (Figure 5). At P6 and P10, terminal myelin loops in the axonal paranodes are still migrating to the paranodal domain from the internodal region (Figure 5a–c). By P14, the paranodes are formed, showing terminal myelin loop heads connected to the paranodal axolemma and juxtaposed closely with no gaps, similar to those seen in young adult cochleas (Figure 5f).

As shown in Figure 5g–I, the terminal loops of the myelin lamellae from satellite cells were not found at the somal side of ganglion nodes until P14, due to the delayed myelination of the soma by the satellite cell (Figure 5g-j). At P14, the paranodal flank generated by a Schwann cell shows clear organization and a tight connection between the terminal myelin loops and the axolemma (Figure 5i). In contrast, the paranodal flank generated by a satellite cell in the ganglion node showed no or incomplete attachment of the lamellae with the paranodal axolemma (Figure 5i). Satellite cell-lamellae are very few and are loosely attached to the axolemma. By 1 M, the number of satellite cell-lamellae increased and the length of unmyelinated node gap between myelinated paranodes decreased compared to P14 (Figure 5j–l). However, the terminal loops of the satellite cell appear only loosely connected to the paranodal axolemma (Figure 5f,l) when compared to the tightly connected terminal loops of the Schwann cell (Figure 5f). Regardless of the age of the AN, the ultrastructural differences were evident between axon-Schwann cell and axon-satellite cell connections. Fewer myelin lamellae from satellite cells surrounded the soma and terminated at the ganglion paranode compared to Schwann cells. Also, high-resolution imaging analysis of

the axonal node and ganglion node showed that cell adhesion molecule Cntn1 was not expressed or only expressed minimally at the somal side of the ganglion node, which may result in a weaker connection between axons and satellite cells (Figure 5m–p), a conclusion supported by our TEM observations (Figure 5J–I) and a previous study (Rosenbluth, 1962). The terminal myelin loop heads, though connected to the axolemma, have much more space between the loops and axolemma, suggesting that axon-satellite connections are weaker than axon-Schwann cell connections (Figure 5o,p).

3.5 | Ganglion and axonal node lengths in the AN are distinctively different during postnatal development

As shown in Figure 5f, j–l, the ganglion node is longer than the axonal node in ANs of young adult mice. To quantify and characterize how these nodes change during development, we measured the axonal (Figure 6a-f) and ganglion (Figure 6g–l) node lengths across the cochlear turns at pre-hearing onset timepoints (P7, P10) and post-hearing onset timepoints (P14, P21, and 1 M) (Table 2). Note that ganglion node lengths were measured from both sides of the somata and animal numbers used in each condition were $n_{P7} = 6$, $n_{P10} = 6$, $n_{P14} = 8$, $n_{P21} = 7$, and $n_{1M} = 8$. While we primarily used the node marker NrCAM for our measurement studies, we also measured axonal and ganglion nodes marked by Nav1.6 and found no significant difference in the measured lengths between the two node markers at P14 (Figure S2; Figure 4). Kruskal Wallis tests corrected for inflated family-wise error using the Benjamini-Hochberg procedure (Benjamini & Hochberg, 1995) found that axonal nodes are significantly longer at P7 compared to P10 and P14 for all cochlear turns (Figure 6a-f). For example, in the middle turn, P7 axonal nodes are approximately 0.4 μm longer than P10 axonal nodes ($p < .0001$) and 0.5 μm longer than P14 axonal nodes ($p < .0001$). This may be due to the relatively large distance between two opposing myelin sheaths in early myelination. As myelination continues, the opposing myelin sheaths formed by two Schwann cells move closer, forming the unmyelinated nodal gap. At P14, the axonal node gap is at its shortest for all three turns. By 1 M, however, the axonal nodes have significantly increased in length compared to P14. The mean node length at P14 was ~1.5 μm, while at 1 M the mean node length had increased to ~1.9 μm across all three turns. An evaluation of how axonal node length changed during development revealed a dynamic pattern that was evident in all three cochlear turns. Nodes were longer at P7, shortened at P14, and then lengthened again at 1 M (Figure 6a-f). Plotted graphically, the temporal profile creates a "V" shape. For the ganglion nodes, the mean length was significantly shorter at P21 than at P7 and P10 (mean diffs. P7 vs. P21 = 0.80 μm, $p < .0001$; P10 vs. P21 = 0.51 μm, $p = .0009$), but was not significantly different from P14 (mean diff. P14 vs. P21 = 0.24, $p = .06$ for the middle turn (Figure 6h,k). In the middle turn, the ganglion node lengths continually shortened with age, from P7 towards 1 M (Figure 6h,k). In the basal turn, the ganglion node continually shortened from P7 to P14, but unexpectedly lengthened again at 1 M (Figure 6i,l).

In contrast to observations in axonal nodes, ganglion nodes are consistently shortened during development (Figure 6g–l). This pattern is clearly defined in the middle turn across the five critical time periods we analyzed, ranging from P7 to 1 M [$F(4,29) = 19.88$, $p < .0001$]. Differences in temporal profiles of axonal and ganglion lengths can be explained, in part,

by the timing of completion of AN myelination, as shown in Figure 1. This explanation is especially true for the ganglion nodes, which have one flanking Schwann-cell paranode and one flanking satellite-cell paranode. Myelination of the somata by satellite cells occurs later than that of the axonal afferents by Schwann cells. We (Figure S1) and others (Petitpré et al., 2018; Shrestha et al., 2018; Sun et al., 2018) found that differentiation of type I SGNs into three molecularly distinct subtypes occurs between P14 and P21. This differentiation may involve molecular and structural changes that further refine nodal microdomains, leading to differential changes in the length of axonal and ganglion nodes. In agreement with the ultrastructural observations described in Figure 5, which suggest that the length of the ganglion node is longer than that of the axon node, our node length measurements show that ganglion nodes are indeed longer than axonal nodes at P7, P10, P14, P21, and 1 M and for all cochlear turns measured (Table 2).

3.6 | The lengths of axonal and ganglion nodes are associated with different aspects of AN function

During nerve development, refinements of either myelin thickness or internode length regulate the conduction speed of myelinated axons (Fields, 2008; Kimura & Itami, 2009). This process is involved in the synchronization of action potentials (Lang & Rosenbluth, 2003). We hypothesized that changes in axonal and ganglion node lengths are critical for AN development, contributing to improvement in AN function and hearing onset. To test this hypothesis, we first performed a comprehensive analysis of AN function at P14 and P21 using multi-metric measurements of ABR wave I, which is generated by the AN (McClaskey et al., 2020). This multi-metric approach, which was first developed for human studies (Harris et al., 2018), assesses different aspects of peripheral auditory function in vivo with an emphasis on suprathreshold hearing and neural synchrony. These measures include intertrial phase coherence (Lachaux et al., 1999), which is an estimate of the consistency of the phase of the response across trials and is also referred to as the phase locking value (PLV). While originally developed for cortical analyses, techniques for quantifying PLV have recently been adapted for analysis of the AN in mice (McClaskey et al., 2020) and humans (Harris et al., 2018; 2021). Using this novel method, we examined suprathreshold AN function including (1) estimates of neural synchrony via phase-locking value (PLV), and (2) ABR wave I peak amplitude (or maximum amplitude) and peak latency and the change in these metrics with increasing level (Figure 7; Table 3). We performed the analyses at P14 and P21, critical time points of myelination and ABR threshold maturation and hearing onset (Figure 1q). For ABR recording, an 11.3 kHz stimulus was selected because changes in nodal length in the apical and middle portions of the cochlear turn were well-defined for both the axonal (Figure 6 b,e) and ganglion (Figure 6 h,k) nodes and because animals across the different time periods demonstrated consistent thresholds and responses in this frequency region. After the recordings for the P14 and P21 mouse groups were completed, cochleae were collected to be used for node length measurements for correlative structure–function analyses.

Before the correlative analyses, the group averaged responses for wave I mean PLV, peak latency, and peak amplitude were compared at each level and analyzed using a two-tailed, Mann–Whitney U test.

(Table S6). Myelination and nodal length development were hypothesized to coincide with faster conduction velocity and greater neural synchrony (shorter latencies and increased PLV, respectively). As predicted, peak latencies of P21 mice are significantly shorter across all intensity levels compared to that of P14 mice (median diff. 90 dB SPL = 0.35 ms; p = .006) (Figure 7c,d). Previous studies found that AN latencies were shorter after hearing onset in BALB/c mice (Song et al., 2006), but synchrony of wave I during the postnatal period of hearing maturation was not determined. As shown in Figure 7a, PLV is a unitless measure with a value between 0 and 1. A value of 0 means no synchrony and a value of 1 means absolute synchrony. At stimulus levels from 80 to 90 dB SPL, the PLVs at P21 are significantly higher than at P14 (median diff. 80 dB = 0.11, p = .021; 90 dB = 0.14, p = .0003), revealing better neural synchrony in the older mice (Figure 7b). Although peak amplitudes across stimulus levels were not significantly different between P14 and P21 (p = 0.69–0.78), the median response is consistently higher across levels at P21 compared to P14 (range median diffs = 0.01–0.07) (Figure 7c,e). The P21 responses, with regards to PLV, latency, and amplitude, are also less variable compared to responses from the P14 group. Increased variability at P14 relative to P21 may be due to individual differences in the temporal pattern of nodal development.

As shown in Figure 6, axonal and ganglion nodes display distinctive length patterns during postnatal development. To address the relationship between nodal lengths and AN function during postnatal development, nodal lengths of the axonal or ganglion nodes measured from the middle turn were tested at P14 and P21 for correlation with three ABR metrics, including peak latency, peak amplitude, and PLV obtained at 11.3 kHz at 90 dB SPL. Pearson's correlation analysis was performed using combined data from both P14 and P21 (a total of 15 mice) (Table 3). Our analyses revealed that shorter peak latency was significantly correlated to longer axonal nodes (r = 0.495; p = .03), whereas no significant correlation was found between the peak latency and length of the ganglion node (r = 0.403; p = .068) (Figure 7f; Figure S3). In addition, the length of the axonal node was strongly correlated with higher PLV, with longer axonal nodes associated with higher PLV (r = 0.545; p = .018) (Figure 7g). Consistent with our hypothesis, these analyses reveal differences in structural development occurring between P14 and P21 and an association between longer axonal nodes and decreases in response latency and stronger synchrony. When we examined the association between AN synchrony and changes of ganglion node structures, no significant correlation between PLV and ganglion node length was identified (Figure S3).

The growth in peak amplitude with stimulus intensity, or the amplitude intensity slope, was evaluated in lieu of peak amplitude as it is less susceptible to factors such as head size that can contribute to differences in amplitude across development. Growth in amplitude with increasing levels is thought to represent the recruitment of synchronized activity from additional nerve fibers, including both higher threshold fibers and off-frequency fibers that are excited due to the spread of excitation along the basilar membrane. We performed correlation analyses using amplitude intensity slope and node length. Our data shows that shortening ganglion nodes (r =0.526, p = .022), but not lengthening axonal nodes (r = 0.370, p = .088), was positively correlated with amplitude growth across increasing intensity levels (Figure 7h; Figure S3). These data suggest that the ganglion node length, but not the axonal node length, contributes to a steeper amplitude intensity slope. Changes in ganglion

node length with development were not associated with latency or PLV. Taken together, these analyses suggest that postnatal development of axonal nodes underlies enhanced speed and synchrony of AN conduction, whereas refinement of ganglion nodes is associated with greater recruitment of AN fibers, possibly representing the recruitment of higher-threshold fibers.

3.7 | Age-related downregulation of nodal-related genes and degeneration of nodes of Ranvier in the peripheral AN

Loss/dysfunction of nodal components and demyelination have been associated with neurological symptoms of aging (Hinman et al., 2006) and diseases such as Guillain-Barré syndrome and multiple sclerosis (Susuki, 2013). The relationship between aging and changes in nodal structures of the AN has yet to be elucidated. We tested the hypotheses that nodal structures undergo age-related pathophysiological alterations and that the alterations differ between nodal structure types. Immunostaining of ANs in young adult and aged mice demonstrated that node structural integrity, as identified by nodal NrCAM and paranodal Cntn1, deteriorates with age in both axonal and ganglion nodes (Figure 8a). Deterioration of AN $Cntn1^{+}$ paranode was also evident in an aged human temporal bone (Figure 8d). RNA-seq profiling of ANs in young-adult and aged mice revealed that 26 of 42 node-related genes (62%) were significantly affected in the aged tissue (Figure 8b, Table S8). Of these affected genes, 23 were downregulated, suggesting the disruption of the nodes of Ranvier in the aged AN. These genes included key voltage-gated ion channels and structural molecules of the node and paranode. In addition, TEM imaging revealed elongation of ganglion nodes in aged mice compared to young-adult mice (Figure 8c). This observation was confirmed by node length measurements, which revealed significantly longer ganglion nodes in the middle turn of ANs in aged mice compared to young-adult mice (Figure 9a). The ganglion nodes were also significantly narrower in both middle and basal turns (Figure 9e,f). However, no significant changes in node length or width occurred in axonal nodes (Figure 9c, d,g,h). Results of unpaired, two-tailed t-tests comparing age-related node dimension changes are detailed in Table S7. In support of our previous observations (Xing et al., 2012), mice with nodal pathologies showed a robust loss of suprathreshold function, as shown by reduced peak amplitudes and PLV in aged mice (Figure S4). These data suggest that nodal pathology contributes to age-related declines in auditory function. Changes in nodal length, particularly in the ganglion node, could emerge as a new key factor in declines in AN function.

4 | DISCUSSION

Our comprehensive morphological analysis has enhanced our understanding of the axonal node and the ganglion node and elucidated how satellite cells and Schwan cells contribute to nodal structural and functional differences. Here we discuss four key findings pertaining to structural and functional aspects of the node of Ranvier in the AN. First, the completion of the molecular assembly of the nodal structures in the cochlea parallels the onset of hearing function during mouse postnatal development. Clustering of node-related gene expression revealed three stages in node formation: (1) Onset of nodal formation at ~P3, (2) complete assembly of structural molecules at ~P14, and (3) further structural maturation between P14 and P21. Transcriptomic findings, together with findings from immunostaining analysis of

key structural and functional proteins, nodal NrCAM, paranodal Cntn1, and VGSC $Na_v1.6$, demonstrate that molecular assembly of the nodes and paranodes was complete by the onset of hearing at approximately P14. Our data also show that NrCAM is present in the basal area as early as P3, which supports its importance for nodal assembly. Previous studies found that NrCAM protein is essential for the initial clustering of VGSCs in forming nodes and for maintaining and restricting this clustering at the nodes (Amor et al., 2014; Custer et al., 2003; Eshed et al., 2005; Feinberg et al., 2010). Our observations also agree with a recent report describing the maturation of VGSC Nav1.6, along with the expression of the anchoring protein Ankyrin G and Caspr in the heminodes and nodes of Ranvier in rat cochleae between P5 and P7 (Kim & Rutherford, 2016). In addition, our data suggest a temporal dependence in the expression of the axo-glial connector protein Cntn1 in Schwann cell-formed paranodes. These observations demonstrate that molecular assembly of the nodal microdomains begins during early postnatal development and is complete shortly after the onset of hearing function.

Second, we define and characterized two types of nodes of Ranvier in the mouse peripheral AN with distinct features in nodal and paranodal microdomains and their associated glial cells. The characteristics of a ganglion node, which include a compact paranodal structure generated by Schwann cells (on the axon side) and a loose paranodal structure provided by satellite cells (on the soma side), were evaluated across the window of development encompassing myelination and hearing onset as well at the stage of age-related degeneration. The unique features of ganglion nodes distinguish them from axonal nodes of the central and peripheral nervous system, such as the nodes of Ranvier of the sciatic nerve, which have provided most of our current knowledge about nodal specializations and biological function of the glial cells in the AN (see reviews by Peters & Vaughn, 1970; Matthew N. Rasband & Peles, 2016; Salzer, 2015).

Our data also revealed temporal and morphometric characteristics that distinguish two cochlear glial cells: satellite cells and Schwann cells, which form the paranodal structure and provide myelin sheathing to the spiral ganglion cell body and axonal processes, respectively. Myelination of the soma and formation of paranodes by satellite cells are delayed compared to myelination of the axon and formation of paranodes by Schwann cells. Satellite cell myelination of the SGN cell body, although multi-layered, is less dense and less compact. This feature is notably visible at the paranodes formed by satellite cells. In other nervous systems, satellite cells regulate a wide range of biological processes. For example, satellite cells support neuronal metabolism due to amino acid, nucleobase, and fatty-acid transporters present on their surfaces (Zeisel et al., 2018). In the dorsal root ganglia, myelinating satellite cells expressed fractalkines, which regulate inflammatory responses associated with hypernociception (Souza et al., 2013). In the trigeminal nerve, inhibition of Kir4.1 expression by satellite cells causes dysfunction in potassium buffering, which leads to pain-like behavior (Vit et al., 2008). In the AN, satellite cells but not Schwann cells also expressed Kir4.1 (Liu et al., 2019), suggesting a critical regulation of satellite cells in AN function. The special feature of the satellite cell-formed paranode in the cochlear nerve (Figures 4,5,6,7) provides the structural support for its regulatory function.

Third, our study reveals that from P14 to 1 M, while AN function continues to improve, the length of the axonal node in the middle turn continues to increase while the length of the ganglion nodes continues to decrease. The middle portion of the cochlea has the highest nerve fiber density per habenular opening and greatest synapse density per IHC compared to those in the apical and basal portions, and the cochlea has developed to focus on hearing at the central frequencies (Ehret, 1983; Liberman & Liberman, 2015; Panganiban et al., 2018). Our analyses found significant structure–function correlations between nodal structures and suprathreshold AN function: longer axonal nodes were associated with shorter conduction time and stronger neural synchrony, whereas shorter ganglion nodes were associated with stronger amplitude growth of the AN response. These structure–function analyses reveal distinct roles of cochlear glial cells in regulating AN function. Ganglion nodes and their associated satellite cells relate to amplitude growth, a suprathreshold function of the AN response, whereas axonal nodes and Schwann cells are responsible for AN conduction speed and neural synchrony, as measured by peak latency and phase-locking of the ABR wave I response. In the optic nerve and cerebral cortical axon of rats, a computational model showed that the length of the node of Ranvier could determine the velocity of myelinated axon conduction (Arancibia-Cárcamo et al., 2017). A longer axonal node could result in an increased number of VGSCs at the node (if the channel expression level is constant), increasing nerve conduction speed. Most interestingly, our findings highlight the functional importance of the ganglion nodal changes during postnatal development. These interesting findings suggest a potential mechanism whereby the ganglion node in the AN contributes to signal modulation, whereas the axonal node is primarily associated with the maintenance of action potential fine structure, which is generated in the first heminode via glutamatergic IHC-SGN synapse (Coate et al., 2019; Hossain et al., 2005; Pujol et al., 1993). A recent electrophysiological study of mouse SGN suggests that signaling transmission via specialized SGNs allows activity- and -voltagedependent modulation, while the fine structure of the action potential waves is sustained axonally (Liu et al., 2021).

To better understand the mechanisms of this striking functional difference between the two types of nodes in the cochlear nerve and their associated glial cells, characterization of the distribution patterns in voltage-gated ion channels in nodal microdomains is needed. Different expression levels of Nav1.6 along the neuron cell body and processes of spiral ganglion were reported in a previous study (Hossain et al., 2005). Using computational modeling, this study concluded that the expression of Nav 1.6 channels at multiple sites along the SGNs contributes to the generation and regeneration of action potentials. The association between ganglion node length and amplitude growth may represent either the recruitment of additional nerve fibers or the optimization of the generation and regeneration of action potentials with repeated stimulation. Based on the observation that improvement of AN supra-threshold function is associated with the refinement of the ganglion node (e.g., the shorter the nodal length the larger the slope of the amplitude growth), we hypothesize that refinement of ganglion nodes is associated with greater recruitment of AN fibers. There are at least two potential mechanisms to account for this prediction. First, the refinement of ganglion nodes occurs together with the improvement of myelination of SGN somata as shown in Figure 1. The bipolar type I SGNs are located within the conduction pathway, requiring that the action potential generated in the first heminode under the IHCs

must be conducted via their electrically excitable membrane. The improvement of somal myelination and refinement of the ganglion nodal elements is necessary for the efficacy of the regeneration of the action potential in the heminodes at both sides of the SGNs. Second, the refinement of the ganglion nodes may also co-occur with structural refinement of subtypes of the SGNs (e.g., high- spontaneous rate [SR], medium-SR and low-SR neurons) between approximately P14 and P21 (Petitpré et al., 2018; Shrestha et al., 2018; Sun et al., 2018). Growth in amplitude with increasing sound level is most typically associated with the recruitment of additional nerve fibers, including fibers with higher thresholds and lower SRs. The change in ganglion node length and steeper amplitude-intensity slope parallels the differentiation of type I auditory fibers into the three different subtypes (Figure S1). Differentiation into multiple type I subtypes may also contribute to the lengthening of axonal nodes post-hearing onset. Further studies using experimentally manipulated approaches (e.g., dysfunction of subtypes of SGNs using genetic manipulation in vivo) will be needed to directly address these interesting hypotheses.

Studies of single-neuron recording from cats (Liberman & Oliver, 1984), gerbils (Schmiedt, 1989), and mice (Taberner & Liberman, 2004) show that SGN subtypes have distinct morphologies associated with their functional properties. Based on detected correlation between SR and AN axon diameter, high-SR/low-threshold fibers have larger axon diameters compared to low-SR/high-threshold fibers (Liberman & Oliver, 1984). Because axon diameter is related to the thickness of myelination, high-SR fibers may be more myelinated than low-SR fibers. Aside from lengthening of the axonal nodes, we also found that the range of axonal node lengths from minimum to maximum is much more variable at P21/1 M than at P14. This finding suggests the presence of the different subtypes, possibly with high-SR axonal nodes on the shorter end of the length spectrum and low-SR axonal nodes on the longer end. Our analysis also found a significant correlation between axonal nodal length and PLV, a measure of synchrony of AN activity. This result suggests further structural maturation of axonal nodes is associated with postnatal development of different AN subtypes. Further studies are needed to measure the nodes from the different neuron subtypes to determine if each SGN subtype is associated with a certain axonal node length.

Finally, we showed an age-dependent downregulation of node-related gene expression and disruption of nodal structures, particularly the ganglion node structures associated with satellite cells, in the mouse cochleae. These effects occurred with declines in suprathreshold function of the AN response. Based on these observations, degeneration and/or dysregulation of cochlear glial cells, especially satellite cells, may contribute to functional declines in the AN associated with aging. Previous studies showed that mice with nodal abnormalities also exhibited reduced hearing sensitivity. Noise exposure caused disruption of myelin and satellite paranodes (Panganiban et al., 2018) and axonal paranodes (Tagoe et al., 2014). Also, transient ablation of glial cells led to disruption of heminodal clustering (Wan & Corfas, 2017). The direct link between abnormal nodal structures, especially that of ganglion nodes, and the declines in multiple components of AN function have yet to be studied. Here, our data suggest that dysregulation of satellite cells and associated degeneration of the ganglion node structure are an important and new mechanism of AN dysfunction in age-related hearing loss and other forms of sensorineural hearing loss.

Supplementary Material

Refer to Web version on PubMed Central for supplementary material.

ACKNOWLEDGMENTS

We thank Juhong Zhu and Nancy Smythe for their excellent technical assistance, and Richard Schmiedt for his help with the system setup of single-trial ABR recording. We also thank Jayne Ahlstrom, Jeffrey Rumschlag, Nathaniel Parsons and Crystal Herron for their comments and editing of the manuscript, and Aileen Shi for her artwork on the schematics of mouse auditory nerve and nodes of Ranvier. This work was supported by National Institutes of Health Grants K18 DC018517 (H.L.), R01DC012058 (H.L.), R56DC012058-06 (H.L), P50DC000422 (H.L., K.C.H.), SFARI Pilot Award #649452 (H.L), R25 GM072643 (C.H. P., K.V.N.), T32 014435 (C.M.M), P30GM103342 (J.L.B.), P20GM103499 (J.L.B.), P30 CA138313, and S10 OD018113 from Cell & Molecular Imaging Shared Resource and Hollings Cancer Center, C06 RR014516 from the Extramural Research Facilities Program of the National Center for Research Resources, and the Medical University of South Carolina Office of the Vice President for Research.

Funding information

Foundation for the National Institutes of Health, Grant/Award Numbers: K18DC018517, P50DC000422, R01DC012058, R56DC012058, P20GM103499; Simons Foundation Autism Research Initiative, Grant/Award Number: Pilot Award #649452

REFERENCES

Akil O, Sun Y, Vijayakumar S, Zhang W, Ku T, Lee CK, Jones S, Grabowski GA, & Lustig LR (2015). Spiral ganglion degeneration and hearing loss as a consequence of satellite cell death in saposin Bdeficient mice. Journal of Neuroscience, 35(7), 3263–3275. 10.1523/JNEUROSCI.3920-13.2015 [PubMed: 25698761]

Alford BR, & Ruben RJ (1963). Physiological, behavioral and anatomical correlates of the development of hearing in the mouse. Annals of Otology, Rhinology & Laryngology, 72(1), 237–247. 10.1177/000348946307200119

Amor V, Feinberg K, Eshed-Eisenbach Y, Vainshtein A, Frechter S, Grumet M, Rosenbluth J, & Peles E (2014). Long-term maintenance of Na+ channels at nodes of Ranvier depends on glial contact mediated by gliomedin and NrCAM. Journal of Neuroscience, 34(15), 5089– 5098. 10.1523/JNEUROSCI.4752-13.2014 [PubMed: 24719088]

Arancibia-Cárcamo IL, & Attwell D (2014). The node of Ranvier in CNS pathology. Acta Neuropathologica, 128(2), 161–175. 10.1007/s00401-014-1305-z [PubMed: 24913350]

Arancibia-Cárcamo IL, Ford MC, Cossell L, Ishida K, Tohyama K, & Attwell D (2017). Node of Ranvier length as a potential regulator of myelinated axon conduction speed. eLife, 6. e23329. 10.7554/eLife.23329

Bao J, & Ohlemiller KK (2010). Age-related loss of spiral ganglion neurons. Hearing Research, 264(1–2), 93–97. 10.1016/j.heares.2009.10.009 [PubMed: 19854255]

Benjamini Y, & Hochberg Y (1995). Controlling the false discovery rate: A practical and powerful approach to multiple testing. Journal of the Royal Statistical Society: Series B (Methodological), 57(1), 289–300. 10.1111/J.2517-6161.1995.TB02031.X

Boyle MET, Berglund EO, Murai KK, Weber L, Peles E, & Ranscht B (2001). Contactin orchestrates assembly of the septate-like junctions at the paranode in myelinated peripheral nerve. Neuron, 30(2), 385–397. 10.1016/S0896-6273(01)00296-3 [PubMed: 11395001]

Brown LN, Xing Y, Noble KV, Barth JL, Panganiban CH, Smythe NM, Bridges MC, Zhu J, & Lang H (2017). Macrophagemediated glial cell elimination in the postnatal mouse cochlea. Frontiers in Molecular Neuroscience, 10, 407. 10.3389/fnmol.2017.00407 [PubMed: 29375297]

Carbon S, Ireland A, Mungall CJ, Shu S, Marshall B, Lewis S, The AmiGO Hub, & The Web Presence Working Group. (2009). AmiGO: Online access to ontology and annotation data. Bioinformatics, 25(2), 288–289. 10.1093/bioinformatics/btn615 [PubMed: 19033274]

Coate TM, Scott MK, & Gurjar M (2019). Current concepts in cochlear ribbon synapse formation. Synapse, 73(5), e22087. 10.1002/syn.22087

Crawford DK, Mangiardi M, Xia X, Lopez-Valdés HE, & Tiwari- Woodruff SK (2009). Functional recovery of callosal axons following demyelination: A critical window. Neuroscience, 164(4), 1407–1421. 10.1016/j.neuroscience.2009.09.069 [PubMed: 19800949]

Custer AW, Kazarinova-Noyes K, Sakurai T, Xu X, Simon W, Grumet M, & Shrager P (2003). The role of the ankyrin-binding protein NrCAM in node of Ranvier formation. Journal of Neuroscience, 23(31), 10032–10039.

Delorme A, & Makeig S (2004). EEGLAB: An open source toolbox for analysis of single-trial EEG dynamics including independent component analysis. Journal of Neuroscience Methods, 134(1), 9–21. 10.1016/j.jneumeth.2003.10.009 [PubMed: 15102499]

Devaux JJ, & Scherer SS (2005). Altered ion channels in an animal model of Charcot-Marie-tooth disease type IA. Journal of Neuroscience, 25(6), 1470–1480. 10.1523/JNEUROSCI.3328-04.2005 [PubMed: 15703401]

Djannatian M, Timmler S, Arends M, Luckner M, Weil MT, Alexopoulos I, Snaidero N, Schmid B, Misgeld T, Möbius W, Schifferer M, Peles E, & Simons M (2019). Two adhesive systems cooperatively regulate axon ensheathment and myelin growth in the CNS. Nature Communications, 10, 4794. 10.1038/s41467-019-12789-z

Ehret G (1976). Development of absolute auditory thresholds in the house mouse (Mus musculus). Journal of the American Audiology Society, 1(5), 179–184 https://europepmc.org/article/med/956003 [PubMed: 956003]

Ehret G (1983). Peripheral anatomy and physiology II. In Willot JF (Ed.), The auditory psychobiology of the mouse (pp. 169–200). Charles C. Thomas https://oparu.uni-ulm.de/xmlui/bitstream/handle/123456789/1205/vts_6692_9192.pdf?sequence=1

El-Badry MM, Ding D, McFadden SL, & Eddins AC (2007). Physiological effects of auditory nerve myelinopathy in chinchillas. European Journal of Neuroscience, 25(5), 1437–1446. 10.1111/j.1460-9568.2007.05401.x

Ervasti JM, & Campbell KP (1993). A role for the dystrophinglycoprotein complex as a transmembrane linker between laminin and Actin. Journal of Cell Biology, 122(4), 809–823. 10.1083/jcb.122.4.809

Eshed Y, Feinberg K, Poliak S, Sabanay H, Sarig-Nadir O, Spiegel I, Bermingham JR, & Peles E (2005). Gliomedin mediates Schwann cell-axon interaction and the molecular assembly of the nodes of Ranvier. Neuron, 47(2), 215–229. 10.1016/j.neuron.2005.06.026 [PubMed: 16039564]

Eylar EH, Brostoff S, Hashim G, Caccam J, & Burnett P (1971). Basic A1 protein of the myelin membrane. The complete amino acid sequence. Journal of Biological Chemistry, 246(18), 5770–5784. 10.1016/S0021-9258(18)61872-1

Feinberg K, Eshed-Eisenbach Y, Frechter S, Amor V, Salomon D, Sabanay H, Peles E, Dupree JL, Grumet M, Brophy PJ, Shrager P, & Peles E (2010). A glial signal consisting of gliomedin and NrCAM clusters axonal Na+ channels during the formation of nodes of Ranvier. Neuron, 65(4), 490–502. 10.1016/j.neuron.2010.02.004 [PubMed: 20188654]

Fields RD (2008). White matter in learning, cognition and psychiatric disorders. Trends in Neurosciences, 31(7), 361–370. 10.1016/j.tins.2008.04.001 [PubMed: 18538868]

Ford MC, Alexandrova O, Cossell L, Stange-Marten A, Sinclair J, Kopp-Scheinpflug C, Pecka M, Attwell D, & Grothe B (2015). Tuning of Ranvier node and internode properties in myelinated axons to adjust action potential timing. Nature Communications, 6(1), 8073. 10.1038/ncomms9073

Hanani M (2005). Satellite glial cells in sensory ganglia: From form to function. Brain Research Reviews, 48(3), 457–476. 10.1016/j.brainresrev.2004.09.001 [PubMed: 15914252]

Hao X, Xing Y, Moore MW, Zhang J, Han D, Schulte BA, Dubno JR, & Lang H (2014). Sox10 expressing cells in the lateral wall of the aged mouse and human cochlea. PLoS One, 9(6), 97389. 10.1371/journal.pone.0097389

Harley RJ, Murdy JP, Wang Z, Kelly MC, Ropp TJF, Park SH, Maness PF, Manis PB, & Coate TM (2018). Neuronal cell adhesion molecule (NrCAM) is expressed by sensory cells in the cochlea and is necessary for proper cochlear innervation and sensory domain patterning during

development. Developmental Dynamics, 247(7), 934–950. 10.1002/DVDY.24629 [PubMed: 29536590]

Harris JJ, & Attwell D (2012). The energetics of CNS white matter. Journal of Neuroscience, 32(1), 356–371. 10.1523/JNEUROSCI.3430-11.2012 [PubMed: 22219296]

Harris KC, Ahlstrom JB, Dias JW, Kerouac LB, McClaskey CM, Dubno JR, & Eckert MA (2021). Neural presbyacusis in humans inferred from age-related differences in auditory nerve function and structure. Journal of Neuroscience, 41, 10293–10304. 10.1523/JNEUROSCI.1747-21.2021

Harris KC, Vaden KI, McClaskey CM, Dias JW, & Dubno JR (2018). Complementary metrics of human auditory nerve function derived from compound action potentials. Journal of Neurophysiology, 119(3), 1019–1028. 10.1152/jn.00638.2017 [PubMed: 29187555]

Hinman JD, Peters A, Cabral H, Rosene DL, Hollander W, Rasband MN, & Abraham CR (2006). Age-related molecular reorganization at the node of Ranvier. Journal of Comparative Neurology, 495(4), 351–362. 10.1002/cne.20886

Hossain WA, Antic SD, Yang Y, Rasband MN, & Morest DK (2005). Where is the spike generator of the cochlear nerve? Voltage-gated sodium channels in the mouse cochlea. Journal of Neuroscience, 25(29), 6857–6868. 10.1523/JNEUROSCI.0123-05.2005 [PubMed: 16033895]

Huang CY-M, Zhang C, Zollinger DR, Leterrier C, & Rasband MN (2017). An αII spectrin-based cytoskeleton rotects large-diameter myelinated axons from degeneration. Journal of Neuroscience, 37(47), 11323–11334. 10.1523/JNEUROSCI.2113-17.2017

Ishibashi T, Ding L, Ikenaka K, Inoue Y, Miyado K, Mekada E, & Baba H (2004). Tetraspanin protein CD9 is a novel paranodal component regulating paranodal junctional formation. Journal of Neuroscience, 24(1), 96–102. 10.1523/JNEUROSCI.1484-03.2004 [PubMed: 14715942]

Jyothi V, Li M, Kilpatrick LA, Smythe N, LaRue AC, Zhou D, Schulte BA, Schmiedt RA, & Lang H (2010). Unmyelinated auditory type i spiral ganglion neurons in congenic Ly5.1 mice. Journal of Comparative Neurology, 518(16), 3254–3271. 10.1002/cne.22398

Kaplan M, Cho M, Ullian E, & Isom L (2001). Differential control of clustering of the sodium channels Nav1.2 and Nav1.6 at developing CNS nodes of Ranvier. Neuron, 30(1), 105–119. 10.1016/S0896-6273(01)00266-5 [PubMed: 11343648]

Kim KX, & Rutherford MA (2016). Maturation of Nav and Kv channel topographies in the auditory nerve spike initiator before and after developmental onset of hearing function. Journal of Neuroscience, 36(7), 2111–2118. 10.1523/JNEUROSCI.3437-15.2016 [PubMed: 26888923]

Kimura F, & Itami C (2009). Myelination and isochronicity in neural networks. Frontiers in Neuroanatomy, 3, 12. 10.3389/neuro.05.012.2009 [PubMed: 19597561]

Klingseisen A, Ristoiu AM, Kegel L, Sherman DL, Rubio-Brotons M, Almeida RG, Koudelka S, Benito-Kwiecinsk SK, Poole RJ, Brophy PJ, & Lyons DA (2019). Oligodendrocyte neurofascin independently regulates both myelin targeting and sheath growth in the CNS. Developmental Cell, 51(6), 730–744.e6. 10.1016/J.DEVCEL.2019.10.016 [PubMed: 31761670]

Kujawa SG, & Liberman MC (2006). Acceleration of age-related hearing loss by early noise exposure: Evidence of a misspent youth. Journal of Neuroscience, 26(7), 2115–2123. 10.1523/JNEUROSCI.4985-05.2006 [PubMed: 16481444]

Kurioka T, Lee MY, Heeringa AN, Beyer LA, Swiderski DL, Kanicki AC, Kabara LL, Dolan DF, Shore SE, & Raphael Y (2016). Selective hair cell ablation and noise exposure lead to different patterns of changes in the cochlea and the cochlear nucleus. Neuroscience, 332, 242–257. 10.1016/j.neuroscience.2016.07.001 [PubMed: 27403879]

Kwon HS, Johnson TV, Joe MK, Abu-Asab M, Zhang J, Chan CC, & Tomarev SI (2013). Myocilin mediates myelination in the peripheral nervous system through ErbB2/3 signaling. Journal of Biological Chemistry, 288(37), 26357–26371. 10.1074/jbc.M112.446138

Lacas-Gervais S, Guo J, Strenzke N, Scarfone E, Kolpe M, Jahkel M, De Camilli P, Moser T, Rasband MN, & Solimena M (2004). BetaIVSigma1 spectrin stabilizes the nodes of Ranvier and axon initial segments. Journal of Cell Biology, 166(7), 983–990. 10.1083/jcb.200408007

Lachaux J, Rodriguez E, Martinerie J, & Varela FJ (1999). Measuring phase synchrony in brain signals. Human Brain Mapping, 8(4), 194– 208. 10.1002/(sici)1097-0193(1999)8:4<194::aidhbm4>3.0.co;2-c [PubMed: 10619414]

Lang EJ, & Rosenbluth J (2003). Role of myelination in the development of a uniform olivocerebellar conduction time. Journal of Neurophysiology, 89(4), 2259–2270. 10.1152/jn.00922.2002 [PubMed: 12611949]

Lang H, Li M, Kilpatrick LA, Zhu J, Samuvel DJ, Krug EL, & Goddard JC (2011). Sox2 up-regulation and glial cell proliferation following degeneration of spiral ganglion neurons in the adult mouse inner ear. JARO, 12(2), 151–171. 10.1007/s10162-010-0244-1 [PubMed: 21061038]

Lang H, Xing Y, Brown LN, Samuvel DJ, Panganiban CH,Havens LT, Balasubramanian S, Wegner M, Krug EL, & Barth JL (2015). Neural stem/progenitor cell properties of glial cells in the adult mouse auditory nerve. Scientific Reports, 5, 13383. 10.1038/srep13383

Li C, Tropak MB, Gerlai R, Clapoff S, Abramow-Newerly W, Trapp B, Peterson A, & Roder J (1994). Myelination in the absence of myelin-associated glycoprotein. Nature, 369(6483), 747–750. 10.1038/369747a0 [PubMed: 7516497]

Liberman LD, & Liberman MC (2015). Dynamics of cochlear synaptopathy after acoustic overexposure. JARO, 16(2), 205–219. 10.1007/s10162-015-0510-3 [PubMed: 25676132]

Liberman MC (1980). Morphological differences among radial afferent fibers in the cat cochlea: An electron-microscopic study of serial sections. Hearing Research, 3(1), 45–63. 10.1016/03785955(80)90007-6 [PubMed: 7400048]

Liberman MC (2015). Hidden Hearing Loss. Scientific American, 313(2), 48–53. 10.1038/scientificamerican0815-48

Liberman MC (2017). Noise-induced and age-related hearing loss: New perspectives and potential therapies. F1000Research, 6, 927. 10.12688/f1000research.11310.1 [PubMed: 28690836]

Liberman MC, & Kujawa SG (2017). Cochlear synaptopathy in acquired sensorineural hearing loss: Manifestations and mechanisms. Hearing Research, 349, 138–147. 10.1016/j.heares.2017.01.003 [PubMed: 28087419]

Liberman MC, & Oliver ME (1984). Morphometry of intracellularly labeled neurons of the auditory nerve: Correlations with functional properties. Journal of Comparative Neurology, 223(2), 163–176. 10.1002/cne.902230203

Lin HW, Furman AC, Kujawa SG, & Liberman MC (2011). Primary neural degeneration in the Guinea pig cochlea after reversible noise-induced threshold shift. JARO, 12(5), 605–616. 10.1007/s10162-011-0277-0 [PubMed: 21688060]

Liu T, Li G, Noble KV, Li Y, Barth JL, Schulte BA, & Lang H (2019). Age-dependent alterations of Kir4.1 expression in neural crest–derived cells of the mouse and human cochlea. Neurobiology of Aging, 80, 210–222. 10.1016/j.neurobiolaging.2019.04.009 [PubMed: 31220650]

Liu W, Liu Q, Crozier RA, & Davis RL (2021). Analog transmission of action potential fine structure in spiral ganglion axons. Journal of Neurophysiology, 126(3), 888–905. 10.1152/jn.00237 [PubMed: 34346782]

Livak KJ, & Schmittgen TD (2001). Analysis of relative gene expression data using real-time quantitative PCR and the 2ΔΔCT method. Methods, 25(4), 402–408. 10.1006/METH.2001.1262 [PubMed: 11846609]

Lopez-Calderon J, & Luck SJ (2014). ERPLAB: An open-source toolbox for the analysis of event-related potentials. Frontiers in Human Neuroscience, 8, 1–14. 10.3389/fnhum.2014.00213 [PubMed: 24474914]

Love MI, Huber W, & Anders S (2014). Moderated estimation of fold change and dispersion for RNA-seq data with DESeq2. Genome Biology, 15(12), 550. 10.1186/s13059-014-0550-8 [PubMed: 25516281]

Luo S, Jaegle M, Li R, Ehring GR, Meijer D, & Levinson SR (2014). The sodium channel isoform transition at developing nodes of Ranvier in the peripheral nervous system: dependence on a Genetic program and myelination-induced cluster formation. Journal of Comparative Neurology, 522(18), 4057–4073. 10.1002/cne.23656

Luck SJ (2014). An introduction to the event-related potential technique (2nd ed.). MIT Press.

McClaskey CM, Panganiban CH, Noble KV, Dias JW, Lang H, & Harris KC (2020). A multi-metric approach to characterizing mouse peripheral auditory nerve function using the auditory brainstem response. Journal of Neuroscience Methods, 346, 108937. 10.1016/j.jneumeth.2020.108937

Ohlemiller KK, Dahl AR, & Gagnon PM (2010). Divergent aging characteristics in CBA/J and CBA/CaJ mouse cochleae. JARO, 11(4), 605–623. 10.1007/s10162-010-0228-1 [PubMed: 20706857]

Orthmann-Murphy JL, Salsano E, Abrams CK, Bizzi A, Uziel G, Freidin MM, Lamantea E, Zeviani M, Scherer SS, & Pareyson D (2009). Hereditary spastic paraplegia is a novel phenotype for GJA12/GJC2 mutations. Brain, 132, 426–438. 10.1093/brain/awn328 [PubMed: 19056803]

Palay SL, Sotelo C, Peters A, & Orkand PM (1968). The axon hillock and the initial segment. Journal of Cell Biology, 38(1), 193–201. 10.1083/jcb.38.1.193

Panganiban CH, Barth JL, Darbelli L, Xing Y, Zhang J, Li H, Noble KV, Liu T, Brown LSN, Schulte BA, Richard S, & Lang H (2018). Noise-induced dysregulation of quaking RNA binding proteins contributes to auditory nerve demyelination and hearing loss. Journal of Neuroscience, 38(10), 2551–2568. 10.1523/JNEUROSCI.2487-17.2018 [PubMed: 29437856]

Paus T, & Toro R (2009). Could sex differences in white matter be explained by g ratio?. Frontiers in Neuroanatomy, 3, 14. 10.3389/NEURO.05.014.2009/BIBTEX [PubMed: 19753325]

Peters A, & Vaughn J (1970). Morphology and development of the myelin sheath. In Myelination. Charles C. Thomas.

Petitpré C, Wu H, Sharma A, Tokarska A, Fontanet P, Wang Y, Helmbacher F, Yackle K, Silberberg G, Hadjab S, & Lallemend F (2018). Neuronal heterogeneity and stereotyped connectivity in the auditory afferent system. Nature Communications, 9(1), 3691. 10.1038/s41467-018-06033-3

Poliak S, Gollan L, Martinez R, Custer A, Einheber S, Salzer JL, Trimmer JS, Shrager P, & Peles E (1999). Caspr2, a new member of the neurexin superfamily, is localized at the juxtaparanodes of myelinated axons and associates with K+ channels. Neuron, 24(4), 1037– 1047. 10.1016/S0896-6273(00)81049-1 [PubMed: 10624965]

Poliak S, & Peles E (2003). The local differentiation of myelinated axons at nodes of Ranvier. Nature Reviews Neuroscience, 4(12), 968–980. 10.1038/nrn1253 [PubMed: 14682359]

Pujol R, Puel JL, D'aldin CG, & Eybalin M (1993). Pathophysiology of the glutamatergic synapses in the cochlea. Acta Oto-Laryngologica, 113(3), 330–334. 10.3109/00016489309135819 [PubMed: 8100108]

Quarles RH, Everly JL, & Brady RO (1973). Evidene for the close association of a glycoprotein with myelin in rat brain. Journal of Neurochemistry, 21(5), 1177–1191. 10.1111/j.1471-4159.1973.tb07573.x [PubMed: 4761704]

R Foundation for Statistical Computing. (2019). R: The R Project for Statistical Computing

Rasband MN, & Peles E (2016). The nodes of Ranvier: Molecular assembly and maintenance. Cold Spring Harbor Perspectives in Biology, 8(3), a020495. 10.1101/cshperspect.a020495

Rasband MN, & Trimmer JS (2001). Subunit composition and novel localization of K+ channels in spinal cord. Journal of Comparative Neurology, 429(1), 166–176. 10.1002/1096-9861(20000101)429:1<166::aid-cne13>3.0.co;2-y

Rasband MN, Trimmer JS, Schwarz TL, Levinson SR, Ellisman MH, Schachner M, & Shrager P (1998). Potassium channel distribution, clustering, and function in remyelinating rat axons. Journal of Neuroscience, 18(1), 36–47. 10.1523/JNEUROSCI.18-01-00036.1998 [PubMed: 9412484]

Rattay F, Potrusil T, Wenger C, Wise AK, Glueckert R, & SchrottFischer A (2013). Impact of morphometry, myelinization and synaptic current strength on spike conduction in human and cat spiral ganglion neurons. PLoS One, 8(11), e79256. 10.1371/journal.pone.0079256

Rios JC, Melendez-Vasquez CV, Einheber S, Lustig M, Grumet M, Hemperly J, Peles E, & Salzer JL (2000). Contactin-associated protein (Caspr) and contactin form a complex that is targeted to the paranodal junctions during myelination. Journal of Neuroscience, 20(22), 8354–8364. [PubMed: 11069942]

Rios JC, Rubin M, St Martin M, Downey RT, Einheber S, Rosenbluth J, Levinson SR, Bhat M, & Salzer JL (2003). Paranodal interactions regulate expression of sodium channel subtypes and provide a diffusion barrier for the node of Ranvier. Journal of Neuroscience, 23(18), 7001–7011. [PubMed: 12904461]

Romand MR, & Romand R (1990). Development of spiral ganglion cells in mammalian cochlea. Journal of Electron Microscopy Technique, 15(2), 144–154. 10.1002/jemt.1060150206 [PubMed: 2355266]

Rosenbluth J (1962). Subsurface cisterns and their relationship to the neuronal plasma membrane. Journal of Cell Biology, 13(3), 405–421. 10.1083/JCB.13.3.405

Rutherford MA, Chapochnikov NM, & Moser T (2012). Spike encoding of neurotransmitter release timing by spiral ganglion neurons of the cochlea. Journal of Neuroscience, 32(14), 4773–4789. 10.1523/JNEUROSCI.4511-11.2012 [PubMed: 22492033]

Salzer JL (2015). Schwann cell myelination. Cold Spring Harbor Perspectives in Biology, 7, a020529. 10.1101/cshperspect.a020529

Schafer DP, Custer AW, Shrager P, & Rasband MN (2006). Early events in node of Ranvier formation during myelination and remyelination in the PNS. Neuron Glia Biology, 2(2), 69–79. [PubMed: 16652168]

Schmiedt RA (1989). Spontaneous rates, thresholds and tuning of auditory-nerve fibers in the gerbil: Comparisons to cat data. Hearing Research, 42(1), 23–35. 10.1016/0378-5955(89)90115-9 [PubMed: 2584157]

Sherman DL, & Brophy PJ (2005). Mechanisms of axon ensheathment and myelin growth. Nature Reviews Neuroscience, 6(9), 683–690. 10.1038/nrn1743 [PubMed: 16136172]

Shrestha BR, Chia C, Wu L, Kujawa SG, Liberman MC, & Goodrich LV (2018). Sensory neuron diversity in the inner ear is shaped by activity. Cell, 174, 1229–1246. 10.1016/j.cell.2018.07.007 [PubMed: 30078709]

Snipes GJ, Suter U, Welcher AA, & Shooter EM (1992). Characterization of a novel peripheral nervous system myelin protein (PMP22/SR13). Journal of Cell Biology, 117(1), 225–238. 10.1083/jcb.117.1.225

Song L, McGee J, & Walsh EJ (2006). Frequency- and level-dependent changes in auditory brainstem responses (ABRs) in developing mice. Journal of the Acoustical Society of America, 119(4), 2242–2257. 10.1121/1.2180533

Sonntag M, Englitz B, Kopp-Scheinpflug C, & Rübsamen R (2009). Early postnatal development of spontaneous and acoustically evoked discharge activity of principal cells of the medial nucleus of the trapezoid body: An in vivo study in mice. Journal of Neuroscience, 29(30), 9510–9520. 10.1523/JNEUROSCI.1377-09.2009 [PubMed: 19641114]

Souza GR, Talbot J, Lotufo CM, Cunha FQ, Cunha TM, & Ferreira SH (2013). Fractalkine mediates inflammatory pain through activation of satellite glial cells. Proceedings of the National Academy of Sciences of the United States of America, 110(27), 11193–11198. 10.1073/pnas.1307445110

Spoendlin H (1984). Factors inducing retrograde degeneration of the cochlear nerve. Annals of Otology, Rhinology and Laryngology, 112, 76– 82. 10.3109/00016487509124683

Sun S, Babola T, Pregernig G, So KS, Nguyen M, Su S-SM, Palermo AT, Bergles DE, Burns JC, & Müller U (2018). Hair cell mechanotransduction regulates spontaneous activity and spiral ganglion subtype specification in the auditory system. Cell, 174(5), 1247– 1263.e15. 10.1016/J.CELL.2018.07.008 [PubMed: 30078710]

Susuki K (2013). Node of Ranvier disruption as a cause of neurological diseases. ASN Neuro, 5(3), 209–219. 10.1042/AN20130025 [PubMed: 23834220]

Susuki K, Chang KJ, Zollinger DR, Liu Y, Ogawa Y, Eshed-Eisenbach Y, Dours-Zimmermann MT, Oses-Prieto JA, Burlingame AL, Seidenbecher CI, Zimmermann DR, Oohashi T, Peles E, & Rasband MN (2013). Three mechanisms assemble central nervous system nodes of Ranvier. Neuron, 78(3), 469–482. 10.1016/j.neuron.2013.03.005 [PubMed: 23664614]

Taberner AM, & Liberman MC (2004). Response properties of single auditory nerve fibers in the mouse. Journal of Neurophysiology, 93(1), 557–569. 10.1152/jn.00574.2004 [PubMed: 15456804]

Tagoe T, Barker M, Jones A, Allcock N, & Hamann M (2014). Auditory nerve perinodal dysmyelination in noise-induced hearing loss. Journal of Neuroscience, 34(7), 2684–2688. 10.1523/JNEUROSCI.3977-13.2014 [PubMed: 24523557]

Tang W, Zhang Y, Chang Q, Ahmad S, Dahlke I, Yi H, Chen P, Paul DL, & Lin X (2006). Connexin29 is highly expressed in cochlear schwann cells, and it is required for the normal development and function of the auditory nerve of mice. Journal of Neuroscience, 26(7), 1991–1999. 10.1523/JNEUROSCI.5055-05.2006 [PubMed: 16481432]

Thakurela S, Garding A, Jung RB, Müller C, Goebbels S, White R, Werner HB, & Tiwari VK (2016). The transcriptome of mouse central nervous system myelin. Scientific Reports, 6, 25828. 10.1038/srep25828

Vit J-P, Ohara PT, Bhargava A, Kelley K, & Jasmin L (2008). Silencing the Kir4.1 potassium channel subunit in satellite glial cells of the rat trigeminal ganglion results in pain-like behavior in the absence of nerve injury. Journal of Neuroscience, 28(16), 4161–4171. 10.1523/JNEUROSCI.5053-07.2008 [PubMed: 18417695]

Wan G, & Corfas G (2017). Transient auditory nerve demyelination as a new mechanism for hidden hearing loss. Nature Communications, 8, 14487. 10.1038/ncomms14487

Woods DF, Hough C, Peel D, Callaini G, & Bryant PJ (1996). Dlg protein is required for junction structure, cell polarity, and proliferation control in drosophila epithelia. Journal of Cell Biology, 134(6), 1469– 1482. 10.1083/JCB.134.6.1469

Xing Y, Samuvel DJ, Stevens SM, Dubno JR, Schulte BA, & Lang H (2012). Age-related changes of myelin basic protein in mouse and human auditory nerve. PLoS One, 7(4), e34500. 10.1371/journal.pone.0034500

Zeisel A, Hochgerner H, Ernfors P, Marklund U, Linnarsson S, Lö P, Johnsson A, Memic F, Van Der Zwan J, Hä Ring M, Braun E, Borm LE, Manno G. La, Codeluppi S, Furlan A, Lee K, Skene N, Harris KD, Hjerling-Leffler J, & Arenas E (2018). Molecular architecture of the mouse nervous system. Cell, 174, 999–1014. 10.1016/j.cell.2018.06.021 [PubMed: 30096314]

Zhang Y, Chen K, Sloan SA, Bennett ML, Scholze AR, O'Keeffe S, Phatnani HP, Guarnieri P, Caneda C, Ruderisch N, Deng S,Liddelow SA, Zhang C, Daneman R, Maniatis T, BarreS BA, & Wu JQ (2014). An RNA-sequencing transcriptome and splicing database of glia, neurons, and vascular cells of the cerebral cortex. Journal of Neuroscience, 34(36), 11929–11947. 10.1523/JNEUROSCI.1860-14.2014

Zonta B, Tait S, Melrose S, Anderson H, Harroch S, Higginson J, Sherman DL, & Brophy PJ (2008). Glial and neuronal isoforms of Neurofascin have distinct roles in the assembly of nodes of Ranvier in the central nervous system. Journal of Cell Biology, 181(7), 1169–1177. 10.1083/jcb.200712154

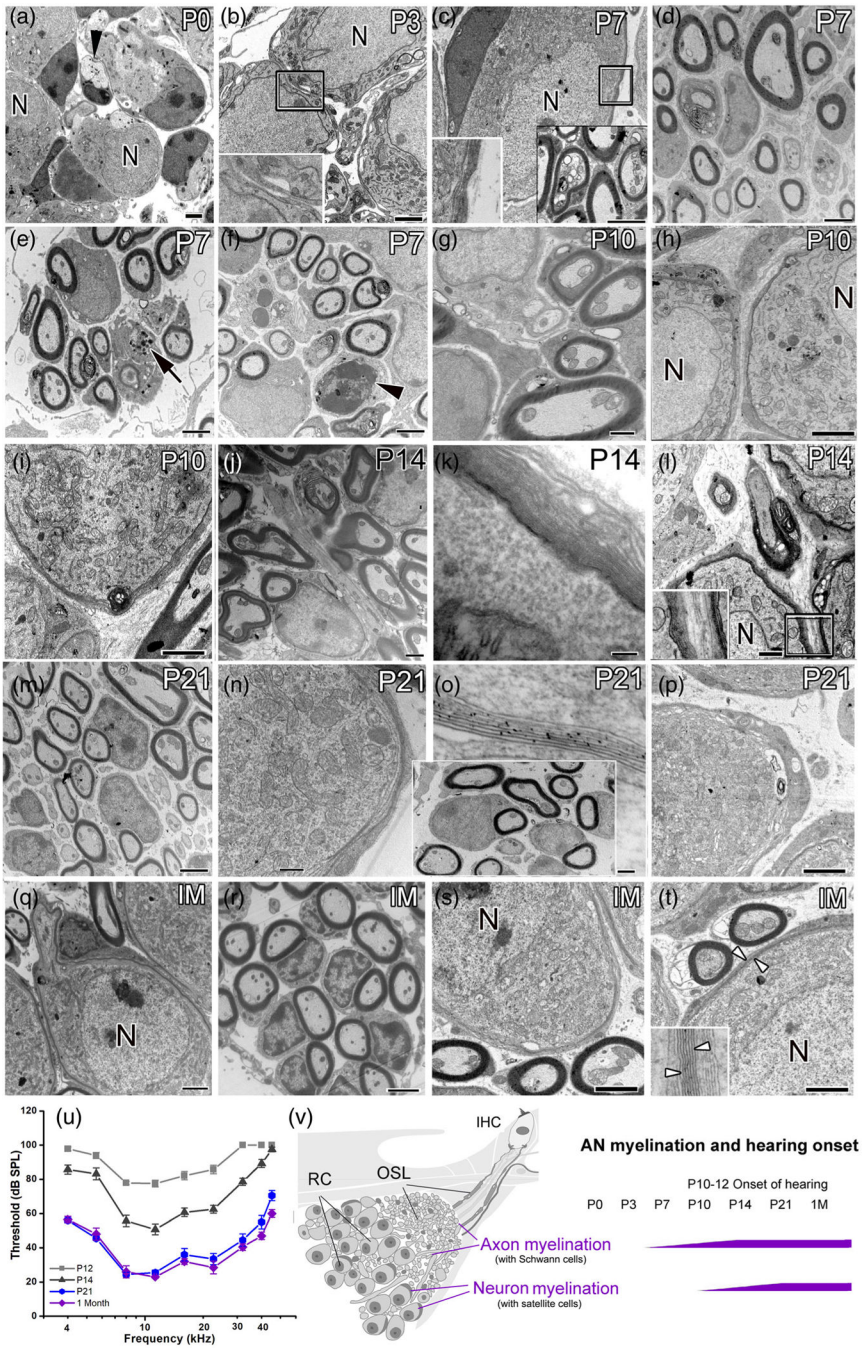

FIGURE 1.

Myelination of the peripheral AN during postnatal development in the CBA/CaJ mouse. (a–t) TEM imaging showed distinct timing and structural features of myelination at ages P0 (a), P3 (b), P7 (c–f), P10 (g–i), P14 (j–l), P21 (m–p), and 1 month (1 M) (q–t). Unmyelinated axons (black arrowhead) and their neuron cell bodies were seen at P0 (a) and P3 (b). Enlargement of boxed area in b shows a thick, single layer of cytoplasm-filled satellite cell process. Schwann cell-associated compact myelin sheaths around AN axons were seen around P7 (bottom-left boxed area in [c]). Compact myelin sheaths were seen

around neurons by P21 (n–p), similar to those at 1 M (q–t). Note that EM graphs in d and the boxed area in o were taken from the basal portion of the cochlea and the remaining images were taken from the middle portion of the cochleas. (u) Auditory brainstem response (ABR) wave I threshold significantly improved from P12 to P21 (mixed-effects model, $p < .0001$). Responses between P21 and 1 M were largely unchanged for most frequencies (see Table S2 for statistical results). Error bars indicate the standard error of the mean in (u). (v) Schematics showing myelinated nerve fibers passing through the osseous spiral lamina (OSL) to innervate inner hair cells (IHC), highlighting the delay of myelination of spiral ganglion somata compared to earlier myelination of axons across postnatal ages. RC, Rosenthal's canal. Scale bars: 2 μm in (a–n), (q–t); 1 μm in (j), (l); 800 nm in (g); 100 nm in (k), (o)

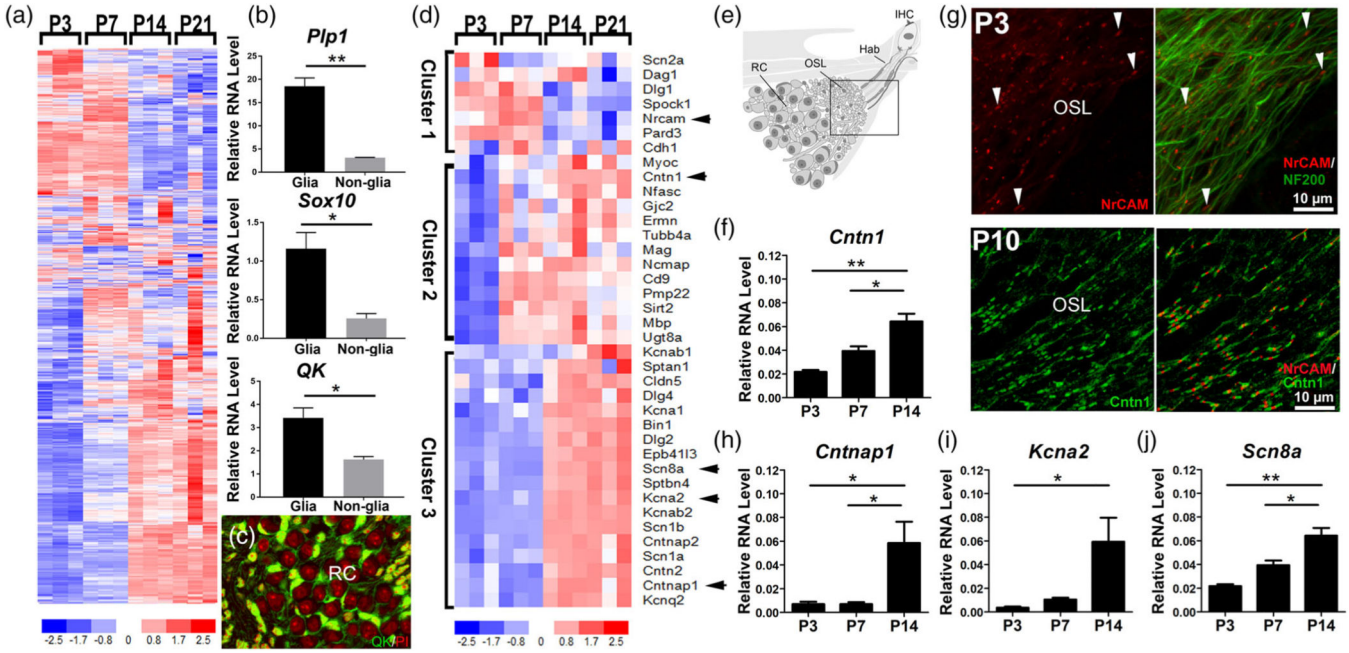

FIGURE 2.

Expression profiles of genes composing nodal structural domains exhibit temporal clustering. (a) Heatmap of myelin-related genes differentially expressed in the AN during development. Of the 1727 myelin-related genes, 1502 were significantly different (*p* adjusted <.05) for at least one of the pairwise comparisons (Table S3). Myelin-related genes used in this analysis were compiled in our previous study (Panganiban et al., 2018). Arrowheads identify genes encoding proteins that are detected in f-J. (b) Validation of myelin related genes *Plp1*, *Sox10*, and *Qk* using RT-qPCR assay (six cochleas from three mice per sample). Glial RNA and nonglial RNA samples were obtained from sorted tdTomato/Plp1^{+} glial cells from AN tissues isolated from tdTomato(+/−)/Plp1-CreER^{T}(+/−) mice at P13-P14 via fluorescent activated cell sorting. (c) Validation of myelin-related molecule QKI (green) using immunostaining with AN cross-sections obtained from young adult CBA/CaJ mice; nuclei labeled with propidium iodide (red); $n = 3$ mice, three cross sections per mouse. (d) Heatmap of node-related genes differentially expressed in AN during postnatal development. Of the 42 node-related genes, 38 were significantly different (*p* adjusted <.05) for at least one pairwise comparison (Table S4). Genes were segregated into three different clusters based on temporal expression profiles. (e) Schematic of the AN. Box indicates the area of immunostaining in (g). OSL, the osseous spiral lamina; Hab, the habenula. Immunostaining shows the presence of nodal NrCAM (red) along axonal processes labeled by NF200 (green) as early as P3 ([g], top panel) and an abundance of axonal nodes with paranodal Cntn1 flanking nodal NrCAM ([g], bottom panel). RT-qPCR experiments validate the presence of nodal (j), paranodal (f, h), and juxtaparanodal (i) genes. One-way ANOVAs with Bonferroni post hoc adjustments were performed to show differential expression among the time points (* = $p < .05$, ** = $p < .01$); $n = 3$ mice per RNA sample per age group

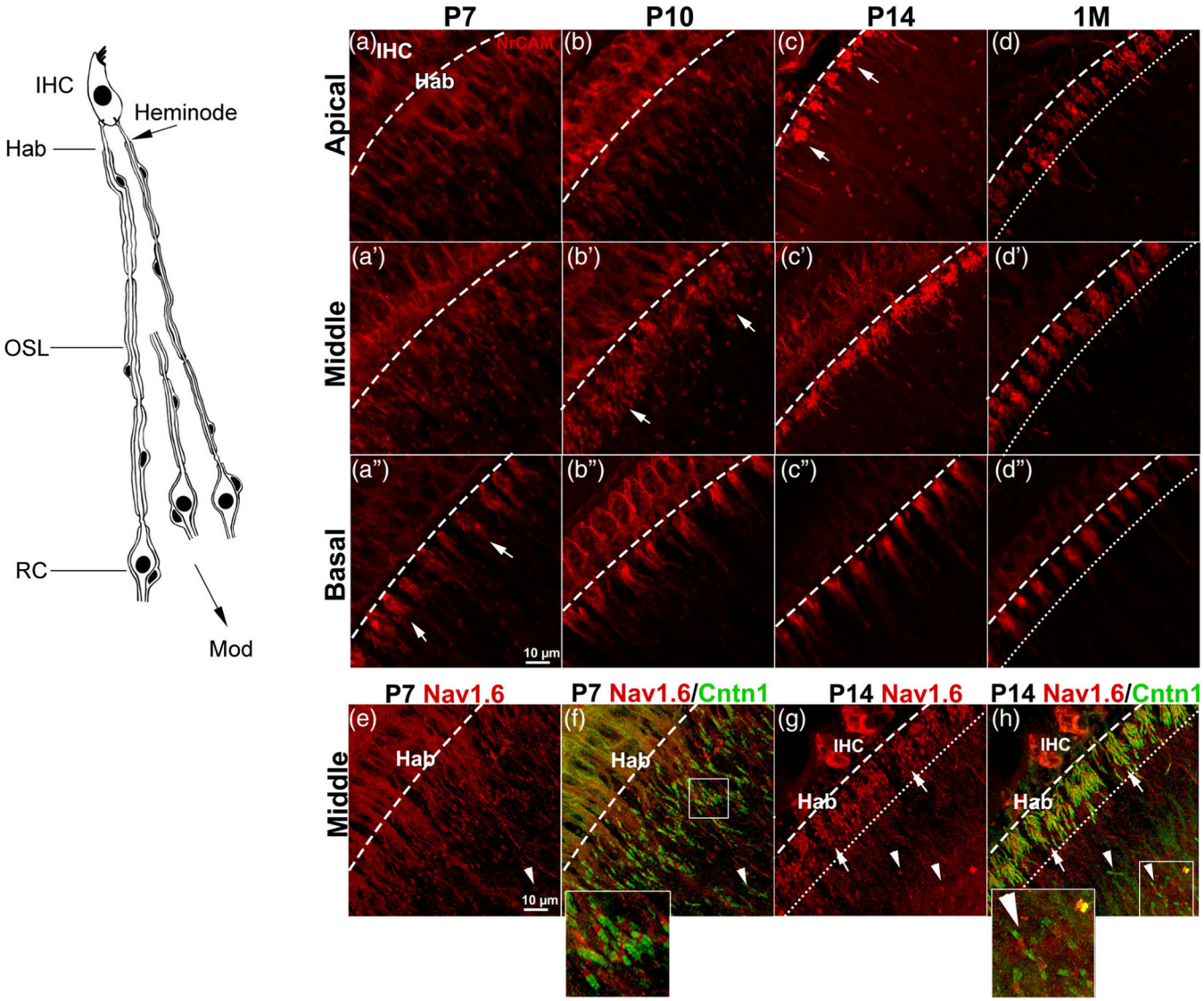

FIGURE 3.

Clustering of AN heminodes across critical timepoints in postnatal development. The left panel is a schematic of peripheral AN fibers illustrating the location of heminodes in the habenula (Hab) and the distal site of the OSL. (a–c) Progression of heminodal clustering indicated by NrCAM immunostaining is shown at critical time points of myelination from the apical (a–d), middle (a'–d'), and basal turn (a"–d"). arrows in a," b,' and c indicate the organized clustering of $NrCAM^{+}$ heminodes of each fiber unit which progress in a basal-to-apical manner. Immunostaining of 1 M ANs in d-d" highlights the well-organized clustering of heminodes (e–f). Dual-immunostaining of nodal Nav1.6 (red) with paranodal Cntn1 (green) shows the progression of heminodal clustering from P7 (e, f) to P14 (g, h). Arrows in (g, h) highlight the completed clustering of heminodes. Arrowheads in (e–h) indicate the first axonal nodes after the heminodal clusters. Enlarged images of the boxed areas in (f, h) were added to the bottoms of (f, h). dashed lines indicate the habenular openings. Dotted lines indicate the space between the habenular opening and the heminodes

most distal to IHCs. These dashed lines and dotted lines were established by observance of the beginning and ending portion of $NrCAM^+$ or $Nav1.6^+$ heminodes, respectively, along with observation of structural landmarks of the habenula and organ of Corti via differential interference contrast microscopy. RC, Rosenthal's canal; mod, modiolus. Scale bars: 10 μm in a" (for a–d"); 10 μm in e (for e–h)

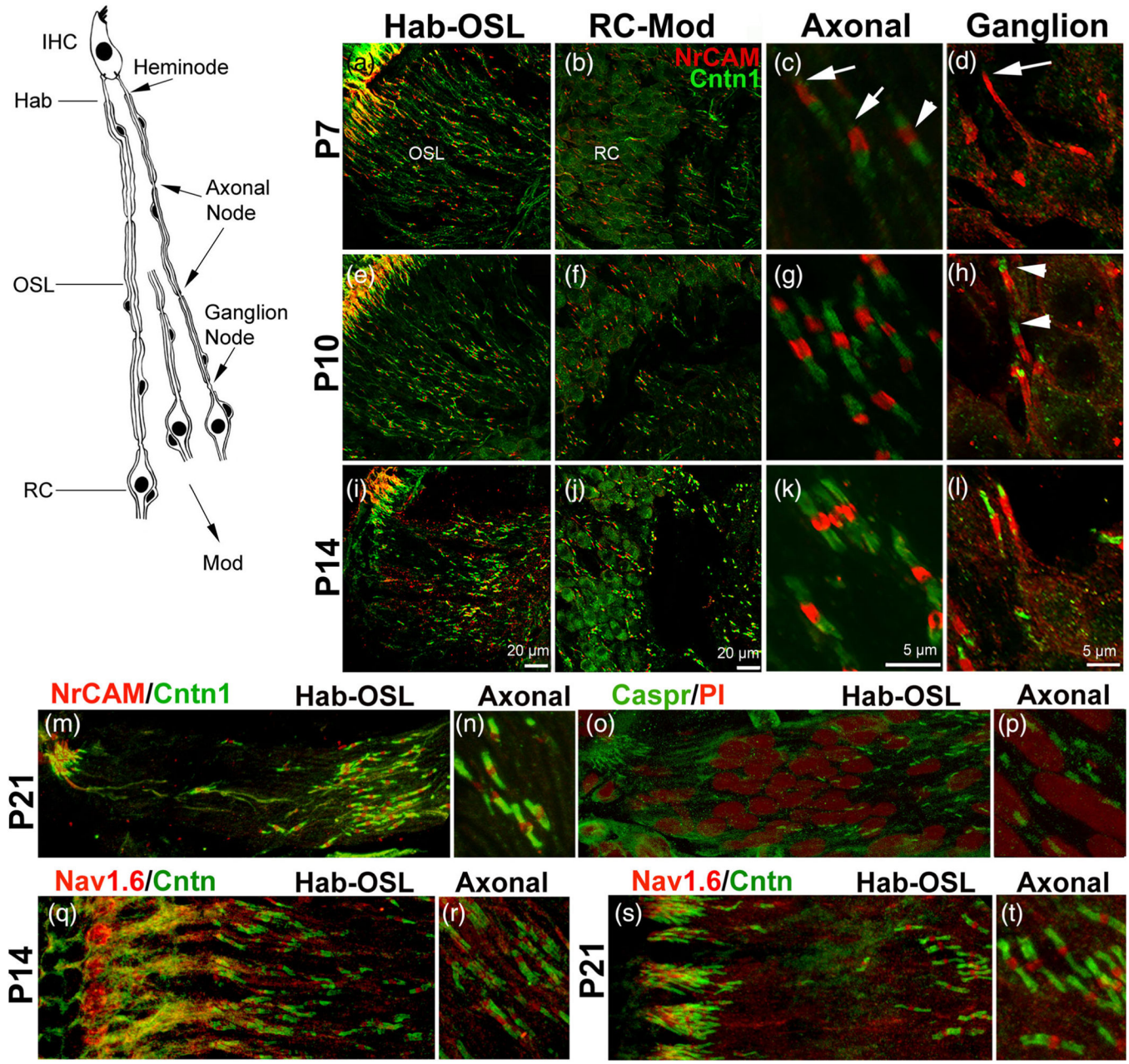

FIGURE 4.

Assembly of nodal and paranodal proteins comprising the axonal and ganglion nodes. The left panel is a schematic illustrating the locations of Hab, OSL, axon nodes within the OSL, and ganglion nodes within RC. (a–l) Panels show the assembly of the $NrCAM^{+}$ nodes (red), and $Cntn1^{+}$ paranodes (green) from P7, P10, and P14. (a, e, i) show heminodes and axonal nodes at the Hab and OSL, respectively. (b, f, j) show ganglion nodes located in RC and the axonal nodes passing through RC to the modiolus. (c, g, k) are enlargements of axonal nodes found in the OSL. White arrows in c indicate axonal nodes with missing undeveloped paranode flanks and the white arrowhead indicates a node completely flanked by two paranodes on either side. (d, h, l) are enlargements of ganglion nodes found in RC.

The white arrow in d indicates a ganglion node without a Cntn1-marked paranodal flank. White arrowheads in h indicate paranode flanks of the ganglion nodes. Images were taken at the middle turn. (m, o) Nodal elements were revealed by NrCAM (m) and Caspr (o) within Hab and OSL at P21. (q,s) Nodal elements were revealed by Nav1.6 within Hab and OSL at P14 (q) and P21 (s). Scale bars: 20 μm in i (for a, e, i); 10 μm in j (for b, f, j); 5 μm in k (for c, g, k); 5 μm in l (f or d, h, l)

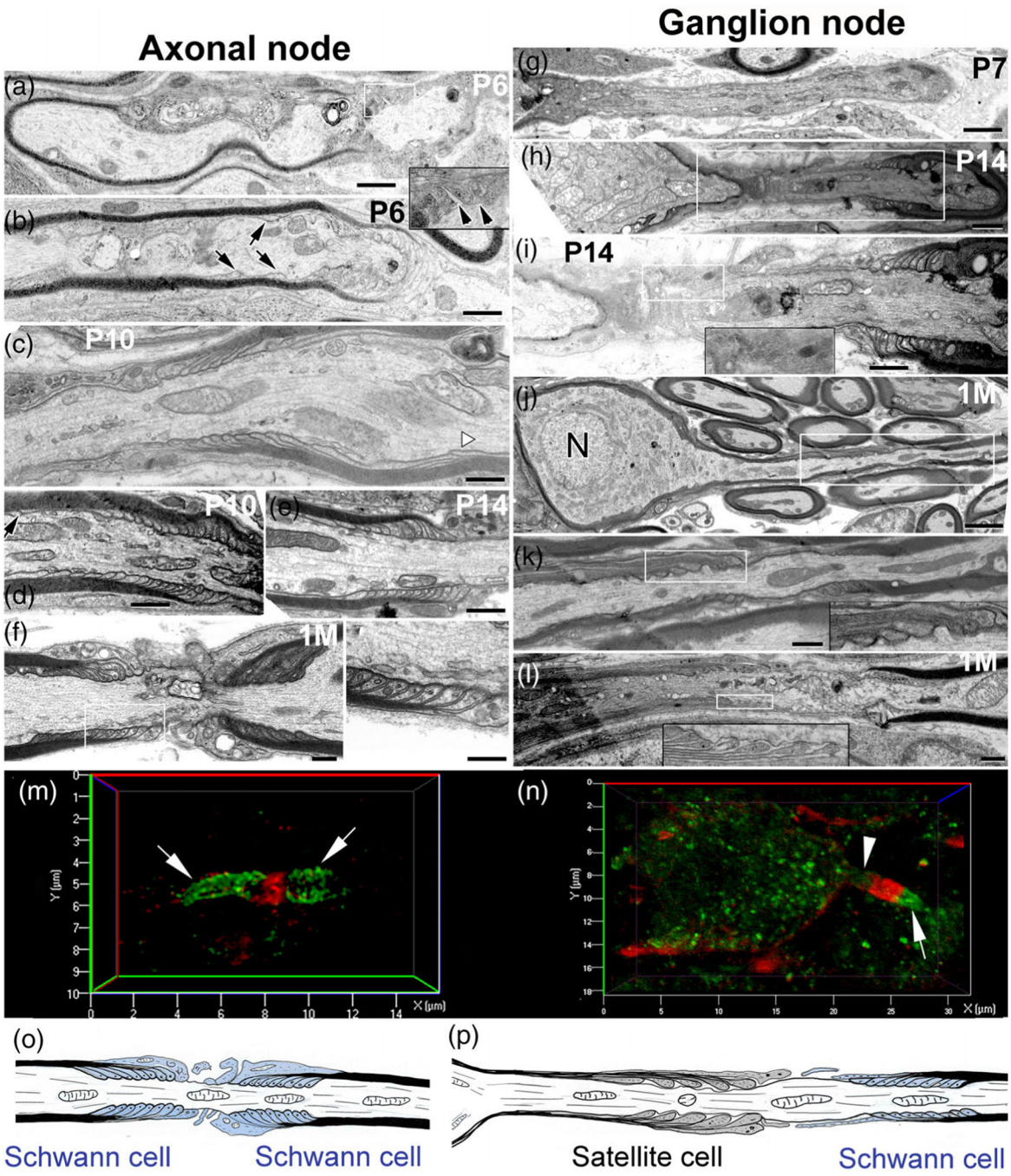

FIGURE 5.

TEM revealing distinct paranodal ultrastructure in the axonal and ganglion nodes. (a–f) Myelin terminal loops at both sides of the axon node assembly by Schwann cells started forming around P6 but were not completed until P10. Terminal loop layers were noncompact (black arrowheads in the enlargement of the white-line-framed boxed area) in a) and several terminal loops are still migrating from the intermodal region (black arrows in [b]). Paranodal domain assembly is mostly complete by P10 (c, d). A white arrowhead in (c) and (a) black arrow in (d) show the terminal loops in the juxtaparanodal domain. Complete, compact

organization of terminal loops at both paranodal domains of the axonal node at P14 (e) is similar to young adult mice (1 M) (f, left panel is an enlargement of boxed area). (g–l) Delayed formation and distinct structure of the paranode (formed by satellite cells) in the somal side of the ganglion node compared to those in the axonal side of the node. Complete assembly of the ganglion node at both sides of the node by satellite cells and Schwann cells occurs by 1 M (j–l). Enlargements of boxed areas in (k), (l) show loose satellite cell terminal loops at the ganglion paranodal domain. (m, n) dual immunostaining with the paranodal marker (NrCAM, red) and nodal maker (Cntn1, green) showed a different structure of axonal (m) and ganglion (n) nodes of a young AN. $NrCAM^+$ paranodal element (arrow) is present at both sides of the axonal node (m) but only one side (axon side) of the ganglion node (n). An arrowhead indicates no $NrCAM^+$ paranodal element at the somal side of the ganglion node. (o, p) Schematics illustrate the distinct structural patterns and glial components of the axonal (o) and ganglion (p) nodes. Scale bars: 400 nm in (a–l); 150 nm in left panel in f; 800 nm in g; 2 μm in (j)

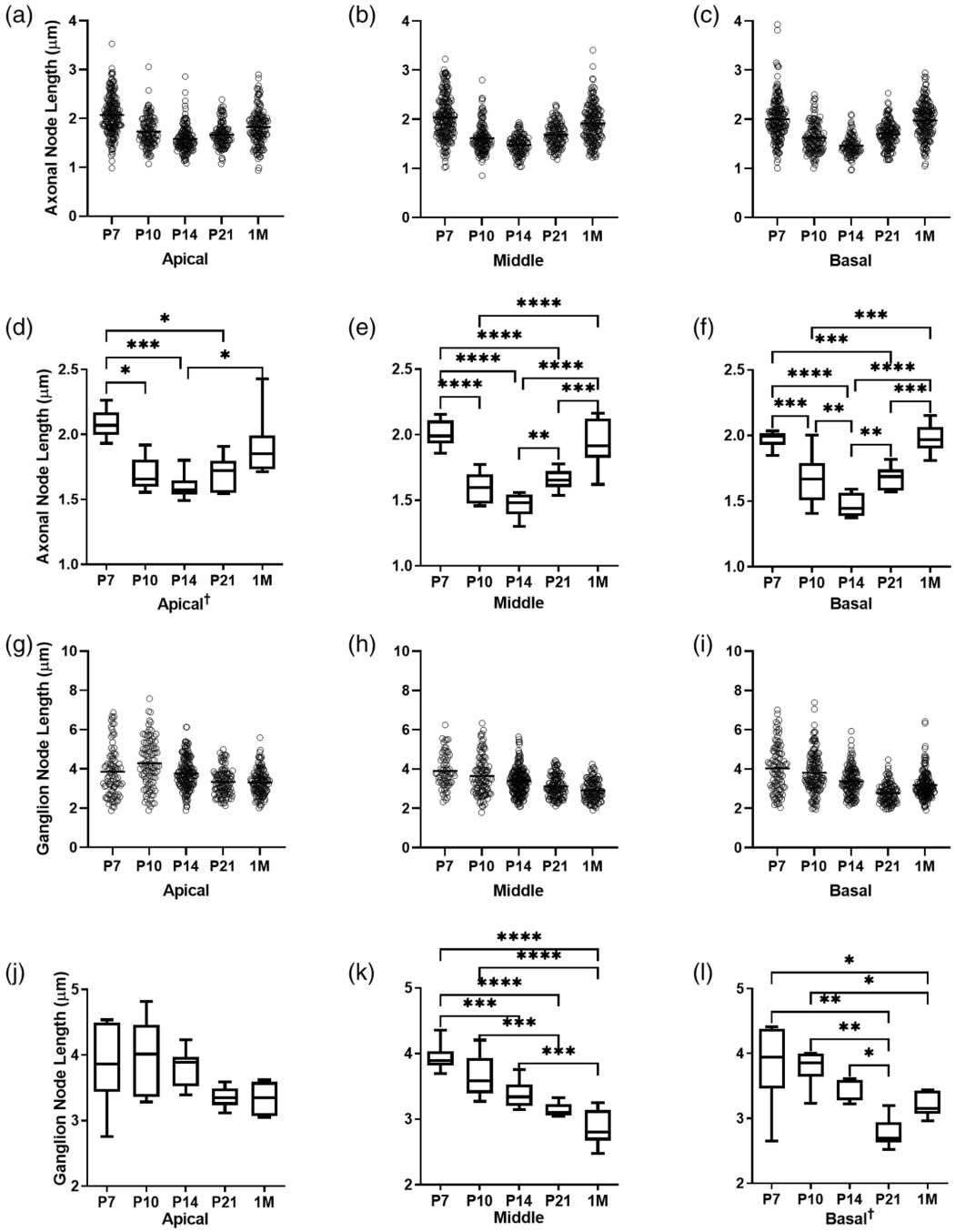

FIGURE 6.

Axonal and ganglion node lengths change between critical developmental time points. Scatter plots show all length measurements taken of axonal (a–c) and ganglion (g–i) nodes in mice from each age group. Box plots show the average length of axonal (d–f) and ganglion (j–l) nodes in mice from each age group. One-way ANOVA with Benjamini-Hochberg post-hoc tests to control for false discovery rate (Q = 0.05) were performed for normally distributed data (e–k). Nonparametric Krusal-Wallis tests with Benjamini Hochberg corrected post-hoc tests were performed for non-normally distributed

data indicated by † (a, l). Bars and asterisks indicate pairwise comparisons with significant discoveries; * = q < 0.05, ** = q < 0.01, *** = q < 0.001, **** = q < 0.0001. n_{P7} = 6, n_{P10} = 6, n_{P14} = 8, n_{P21} = 7, n_{1M} = 8. Average nodal lengths and statistical test results are shown in Table 2

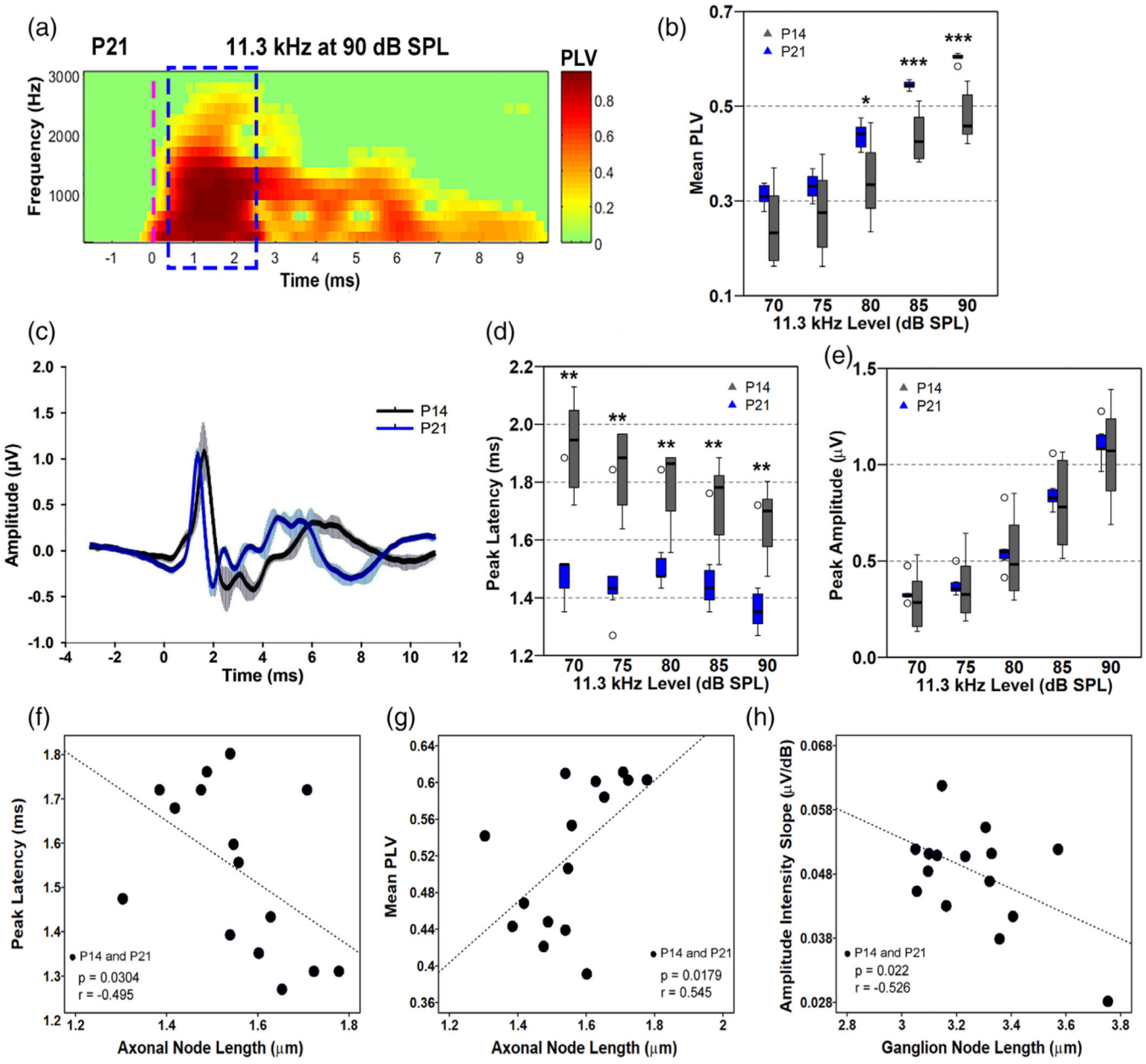

FIGURE 7.

Improvement of AN function evaluated by multiple metrics of ABR and correlation analyses between nodal lengths and ABR metrics. (a) A representative example of a time-frequency heatmap of phase-locking value (PLV) in a mouse at P21. Dashed blue outline indicates the 2-ms window enclosing wave I where data was collected. The green shade is baseline, whereas the shading from yellow to red indicates greater phase-locking. A dashed vertical magenta line indicates stimulus onset. (b) Measurements of AN wave I mean PLV between P14 and P21. Synchrony of AN firing of P21 mice is significantly better than in P14 mice at 80–90 dB SPL. (c) Group-averaged waveforms of the ABR at P14 (gray) and P21 (blue) to an 11.3 kHz tone pip at 90 dB SPL; n = 4 mice/group. (d, e) Measurements of wave I peak latency (d) and amplitude (e) between P14 and P21. Peak latencies at P21

are shorter than that of P14. Peak amplitudes are slightly higher in P21 animals but are not significantly different compared to P14 mice. Two-tailed, Mann–Whitney tests were performed per intensity level between P14 and P21 on b,d, e; $n_{(P14)} = 8$ mice, $n_{(P21)} = 7$ mice. Outliers are indicated by open circles. Data points falling beyond 2 SD from the mean were classified as outliers. * = $p < .05$, ** = $p < .01$, *** = $p < .001$. (f–h) Correlational analyses performed using responses at 90 dB SPL from both P14 and P21 mice, showing significant correlations between the length of axonal nodes and peak latency (f), between the length of the axonal node and mean PLV (g), and between the length of ganglion node and amplitude intensity slope (h). Results of the correlational analysis are included in Table 3

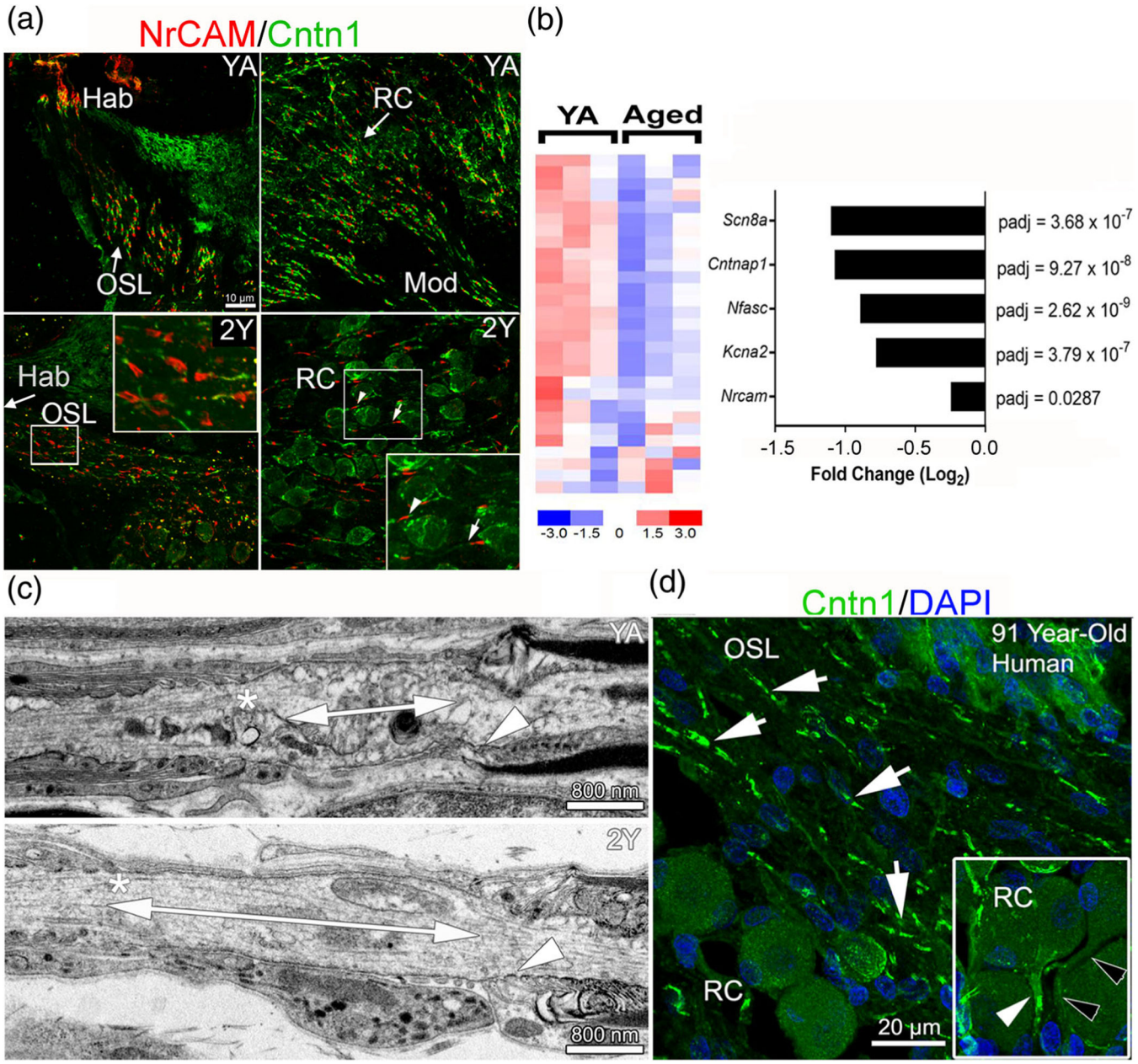

FIGURE 8.

Nodal structures are disrupted in aged ANs. (a) Immunostaining for nodal NrCAM and paranodal Cntn1 in ANs of control (YA) and 2-year-old (2Y) mice. Heminodes at Hab are sparser in 2Y than in YA (middle right). Axonal node structures are disrupted, with some missing paranodal Cntn1 flanks (bottom-left). The presence of Cntn1 also decreased in some ganglion paranodes (arrow, bottom right) compared to others (arrowhead). (b) Expression profiles of differentially expressed node-related genes show significantly reduced expression with aging compared to YA. The bar graph on the right highlights the negative fold change of several node-related genes of interest; $n = 3$ mice/group. (c) TEM imaging revealed an elongated ganglion node in aged (bottom) compared to YA mice (top) as shown by double-ended arrows. Asterisks indicate the satellite cell paranode and arrowheads indicate the

Schwann cell paranode. (d) Immunostaining for Cntn1 and DAPI in aged human temporal bone showed paranodal flanks (arrows) in human AN. Insert shows Cntn1 in the fiber region preceding the SGN soma (white arrowhead) and another similar fiber region lacking Cntn1 reactivity (black arrowheads)

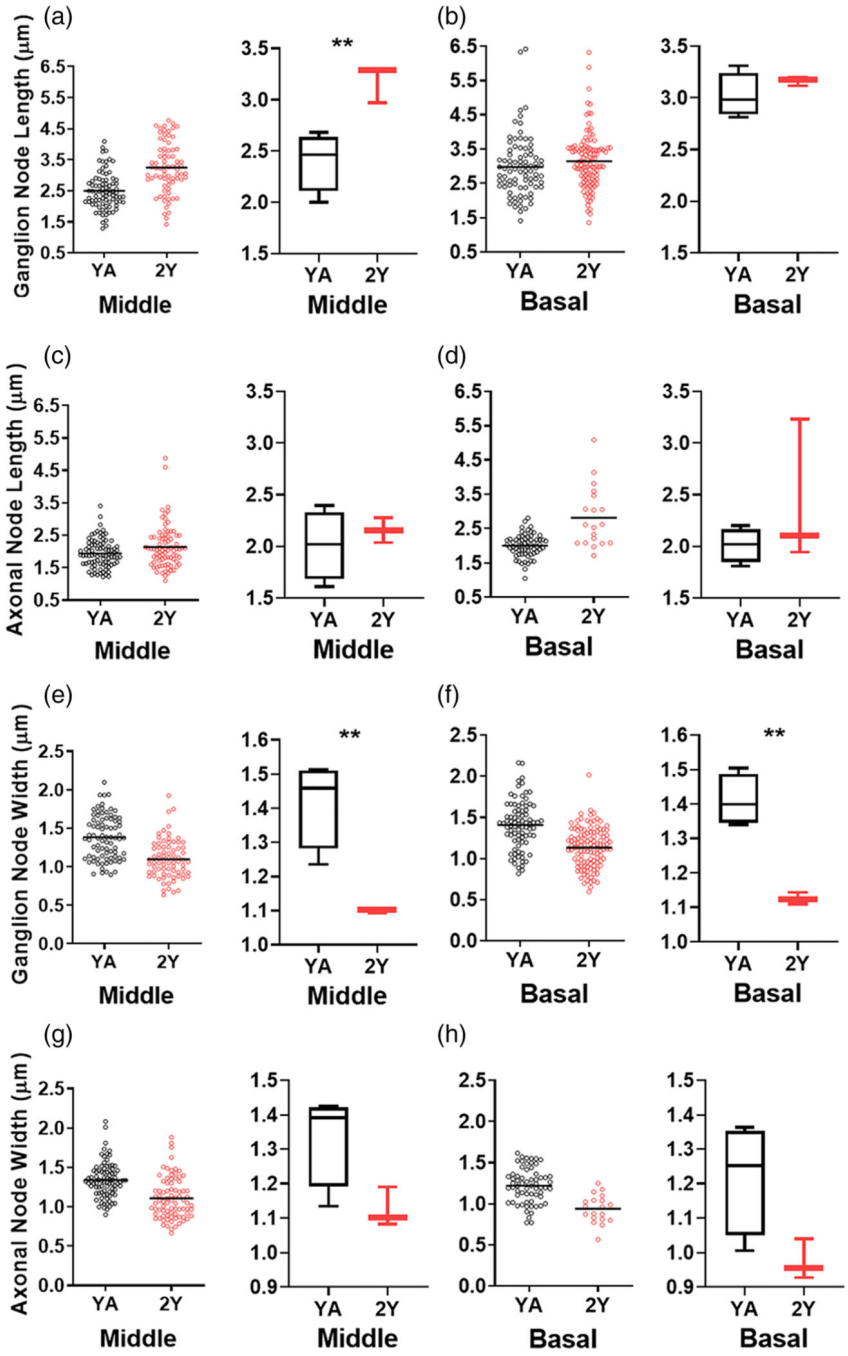

FIGURE 9.

(a–h) Measurements of axonal and ganglion node lengths and widths from YA and 2Y ANs. Ganglion node lengths are significantly increased in the middle cochlear turns of 2Y compared to YA and ganglion node widths are significantly decreased in middle and basal turns of 2Y compared to YA. Unpaired, two-tailed t-test, ** = $p < .01$; $n_{YA} = 4$ mice, $n_{2Y} = 3$ mice. Statistical results are detailed in Table S8

TABLE 1

One-way ANOVA with Bonferroni's post hoc adjustment of relative RNA concentrations of key nodal genes across postnatal ages

Gene	ANOVA *p* value	DF_n, DF_d	F	Comparisons	Mean diff.	95% CI	Adjusted *p* value
Cntn1	.002	2, 6	23.060	P3 vs. P7	−0.018	−0.038–0.003	ns
				P3 vs. P14	−0.043	−0.063–−0.022	≤.05
				P7 vs. P14	−0.025	−0.046–−0.004	≤.01
Cntnap1	.02	2, 6	8.048	P3 vs. P7	−0.0001	−0.049–0.049	ns
				P3 vs. P14	−0.051	−0.100–−0.003	≤.05
				P7 vs. P14	−0.051	−0.100–−0.003	≤.05
Kcna2	.03	2, 6	6.634	P3 vs. P7	−0.007	−0.062–0.048	ns
				P3 vs. P14	−0.056	−0.110–−0.001	≤.05
				P7 vs. P14	−0.049	−0.100–0.006	ns
Scn8a	.002	2, 6	23.060	P3 vs. P7	−0.018	−0.038–−0.003	ns
				P3 vs. P14	−0.043	−0.063–−0.022	≤.01
				P7 vs. P14	−0.025	−0.046–−0.004	≤.05

Abbreviations: CI, confidence intervals; DF_n, degrees of freedom in numerator; DF_d, degrees of freedom in denominator.

TABLE 2

Measurements of axonal and ganglion node length

Mean axonal node length (μm)						
	Apical		**Middle**		**Basal**	
P7	2.08 ±0.11		2.01 ± 0.10		1.97 ± 0.07	
P10	1.69 ± 0.13		1.60 ± 0.12		1.67 ± 0.20	
P14	1.60 ± 0.10		1.46 ± 0.09		1.47 ± 0.09	
P21	1.69 ± 0.14		1.66 ± 0.08		1.68 ± 0.09	
1 M	1.91 ±0.25		1.95 ± 0.19		1.98 ± 0.11	
Mean ganglion node length (μm)						
	Apical		**Middle**		**Basal**	
P7	3.86 ± 0.65		3.94 ± 0.22		3.84 ± 0.64	
P10	3.98 ± 0.58		3.65 ± 0.34		3.79 ± 0.29	
P14	3.81 ± 0.28		3.38 ± 0.20		3.40 ± 0.17	
P21	3.36 ± 0.16		3.14 ± 0.10		2.79 ± 0.23	
1M	3.34 ± 0.22		2.88 ± 0.27		3.20 ± 0.18	
Mean difference between axonal and ganglion node length (μm) by cochlear turn and age						
	Difference Apical	**SE**	**Difference Middle**	**SE**	**Difference Basal**	**SE**
P7	−1.78†	0.27	−1.93‡	0.10	−1.87†	0.26
P10	−2.28†	0.24	−2.06‡	0.15	−2.12‡	0.14
P14	−2.21‡	0.11	−1.91‡	0.08	−1.93‡	0.07
P21	−1.67‡	0.08	−1.48‡	0.05	−1.10‡	0.09
1 M	−1.43‡	0.13	−0.93†	0.12	1.22‡	0.08

Note: Unpaired *t* test

† $p < .0001$

‡ $p < .00001$. SE, standard error.

TABLE 3

Pearson product–moment correlation analyses

			95% confidence interval		
Axonal node length	***r***	***p***	**Lower**	**Upper**	
Peak latency	−0.495	.030	−0.871	−0.038	*
Mean PLV	0.545	.018	0.120	0.880	*
Amplitude intensity slope	0.370	.088	−0.116	0.700	
Ganglion node length					
Peak latency	0.403	.068	−0.017	0.745	
Mean PLV	−0.364	.091	−0.788	0.213	
Amplitude intensity slope	−0.526	.022	−0.855	0.217	†

Note: $n = 15$. All tests were 1-tailed. 95% confidence intervals were computed from a bootstrap protocol that resampled the data 1000 times.

*$p < .05$ and the 95% confidence interval does not cross 0.

†Either $p < .05$ or the 95% confidence interval does not cross 0.